LETTER

Multifunctional ferrofluid–infused surfaces with reconfigurable multiscale topography

Wendong Wang[1,2,3,13], Jaakko V. I. Timonen[1,4,13], Andreas Carlson[1,2,5], Dirk-Michael Drotlef[3], Cathy T. Zhang[1,2], Stefan Kolle[1], Alison Grinthal[1], Tak-Sing Wong[1,2,8], Benjamin Hatton[1,2,9], Sung Hoon Kang[1,2,10], Stephen Kennedy[1,2,11], Joshua Chi[1,6,12], Robert Thomas Blough[2], Metin Sitti[3], L. Mahadevan[1,2,7] & Joanna Aizenberg[1,2,6,7]*

Developing adaptive materials with geometries that change in response to external stimuli provides fundamental insights into the links between the physical forces involved and the resultant morphologies and creates a foundation for technologically relevant dynamic systems[1,2]. In particular, reconfigurable surface topography as a means to control interfacial properties[3] has recently been explored using responsive gels[4], shape-memory polymers[5], liquid crystals[6–8] and hybrid composites[9–14], including magnetically active slippery surfaces[12–14]. However, these designs exhibit a limited range of topographical changes and thus a restricted scope of function. Here we introduce a hierarchical magneto-responsive composite surface, made by infiltrating a ferrofluid into a microstructured matrix (termed ferrofluid-containing liquid-infused porous surfaces, or FLIPS). We demonstrate various topographical reconfigurations at multiple length scales and a broad range of associated emergent behaviours. An applied magnetic-field gradient induces the movement of magnetic nanoparticles suspended in the ferrofluid, which leads to microscale flow of the ferrofluid first above and then within the microstructured surface. This redistribution changes the initially smooth surface of the ferrofluid (which is immobilized by the porous matrix through capillary forces) into various multiscale hierarchical topographies shaped by the size, arrangement and orientation of the confining microstructures in the magnetic field. We analyse the spatial and temporal dynamics of these reconfigurations theoretically and experimentally as a function of the balance between capillary and magnetic pressures[15–19] and of the geometric anisotropy of the FLIPS system. Several interesting functions at three different length scales are demonstrated: self-assembly of colloidal particles at the micrometre scale; regulated flow of liquid droplets at the millimetre scale; and switchable adhesion and friction, liquid pumping and removal of biofilms at the centimetre scale. We envision that FLIPS could be used as part of integrated control systems for the manipulation and transport of matter, thermal management, microfluidics and fouling-release materials.

Whereas the magnetic field-induced reconfiguration of a ferrofluid to form macroscopic protuberances on a flat surface is well known[15,16], the behaviour of a ferrofluid in a microstructured confinement might elicit a range of otherwise unachievable multiscale topographical responses, enabled by the capillary pressure within the porous substrate (Fig. 1a). To explore this concept, we used various microstructured substrates (see Table 1) infiltrated with fluorocarbon- or silicone-oil-based ferrofluids. A small permanent magnet was placed under the samples and the resulting spatiotemporal changes in surface topography were visualized using an angled illumination technique. The thickness of the ferrofluid overlayer was measured using a force probe (see Extended Data Fig. 1) and the evolution of the profile of the ferrofluid–air interface was measured using a laser scanning microscope (Extended Data Fig. 2a, b).

The non-uniform magnetic field created by the magnet initiates three sequential and interrelated processes to generate dynamic multiscale topographies (Fig. 1b). In the first step, the magnetic field causes a withdrawal of the initially flat ferrofluid overlayer above the microstructures. Withdrawal leads to the formation of a macroscopic protuberance with lateral size comparable to that of the magnet (about 1–20 mm). In the second step, the ferrofluid that remains trapped in the microstructured matrix through capillary force is pulled out of the pores by a magnetic pressure $|p_m| \approx \mu_0 M_s H_0$ (Extended Data Fig. 3a–c), where μ_0 (in units of N A^{-2}) is the vacuum permeability, M_s (A m^{-1}) is the saturation magnetization of the ferrofluid and H_0 (A m^{-1}) the strength of the applied magnetic field[15]. The magnetic pressure is counteracted by the capillary pressure $p_\gamma \approx 2\gamma/d_y$, where γ is the surface tension of the ferrofluid–air interface and $d_y/2$ is half the width of the channels and the largest characteristic radius of the porous matrix. If $|p_m| \leq p_\gamma$, then ferrofluid will remain trapped in the pores (Extended Data Fig. 3e–g). If $|p_m| > p_\gamma$, such as for the case shown in Fig. 1b and Extended Data Fig. 3d, where $|p_m| \approx 10^4$ Pa and $p_\gamma \approx 10^3$ Pa, then ferrofluid will be extracted from the pores, leading to the appearance of the conformally coated micro-topographical region (1) (Fig. 1a). In the third step, the micro-topographical area expands outwards through porous-capillary flow, while the macroscopic protuberance continues to grow through the accumulation of ferrofluid. The initial extraction of ferrofluid from the areas around the magnet deforms the ferrofluid–air interface, producing a capillary pressure even in areas far from the magnet where the magnetic pressure is smaller than the capillary pressure. The interface has a gradually increasing height along the channel, from its minimum near the magnet to its maximum height h_0 far away from the magnet (Fig. 1c, Extended Data Fig. 2a). The combination of the magnetic and capillary pressures makes the flow follow the micro-topography, even in highly complex channel geometries such as the spiral shape of pattern 6 (Table 1), where the flow makes turns along a curved path (see Extended Data Fig. 2e).

The size of the micro-topographical area, characterized by its length along the micro-channels L_x (shown in state (iv) of Fig. 1b), was observed to scale with time as $L_x \propto t^{0.35-0.5}$ for different patterns and overlayer thicknesses (Fig. 1d, Extended Data Fig. 2c, d). By balancing the rate of change of work done by the capillary force with the viscous dissipation, we obtain

$$\gamma \dot{L}_x d_y \approx \gamma d_y U \approx \int \eta \left(\frac{\partial U}{\partial z} \right)^2 \mathrm{d}V \approx \eta \left(\frac{U}{h_0} \right)^2 h_0 L_x d_y \qquad (1)$$

[1]John A. Paulson School of Engineering and Applied Sciences, Harvard University, Cambridge, MA, USA. [2]Wyss Institute for Biologically Inspired Engineering, Harvard University, Cambridge, MA, USA. [3]Max Planck Institute for Intelligent Systems, Stuttgart, Germany. [4]Department of Applied Physics, Aalto University School of Science, Espoo, Finland. [5]Department of Mathematics, Mechanics Division, University of Oslo, Oslo, Norway. [6]Department of Chemistry and Chemical Biology, Harvard University, Cambridge, MA, USA. [7]Kavli Institute for Bionano Science and Technology, Harvard University, Cambridge, MA, USA. [8]Present address: Department of Mechanical and Nuclear Engineering and the Materials Research Institute, The Pennsylvania State University, University Park, PA, USA. [9]Present address: Materials Science and Engineering, University of Toronto, Toronto, Ontario, Canada. [10]Present address: Department of Mechanical Engineering, Hopkins Extreme Materials Institute, Johns Hopkins University, Baltimore, MD, USA. [11]Present address: Department of Biomedical and Chemical Engineering, University of Rhode Island, Kingston, RI, USA. [12]Present address: Department of Chemical and Biomolecular Engineering, Johns Hopkins University, Baltimore, MD, USA. [13]These authors contributed equally: Wendong Wang, Jaakko V. I. Timonen. *e-mail: jaiz@seas.harvard.edu
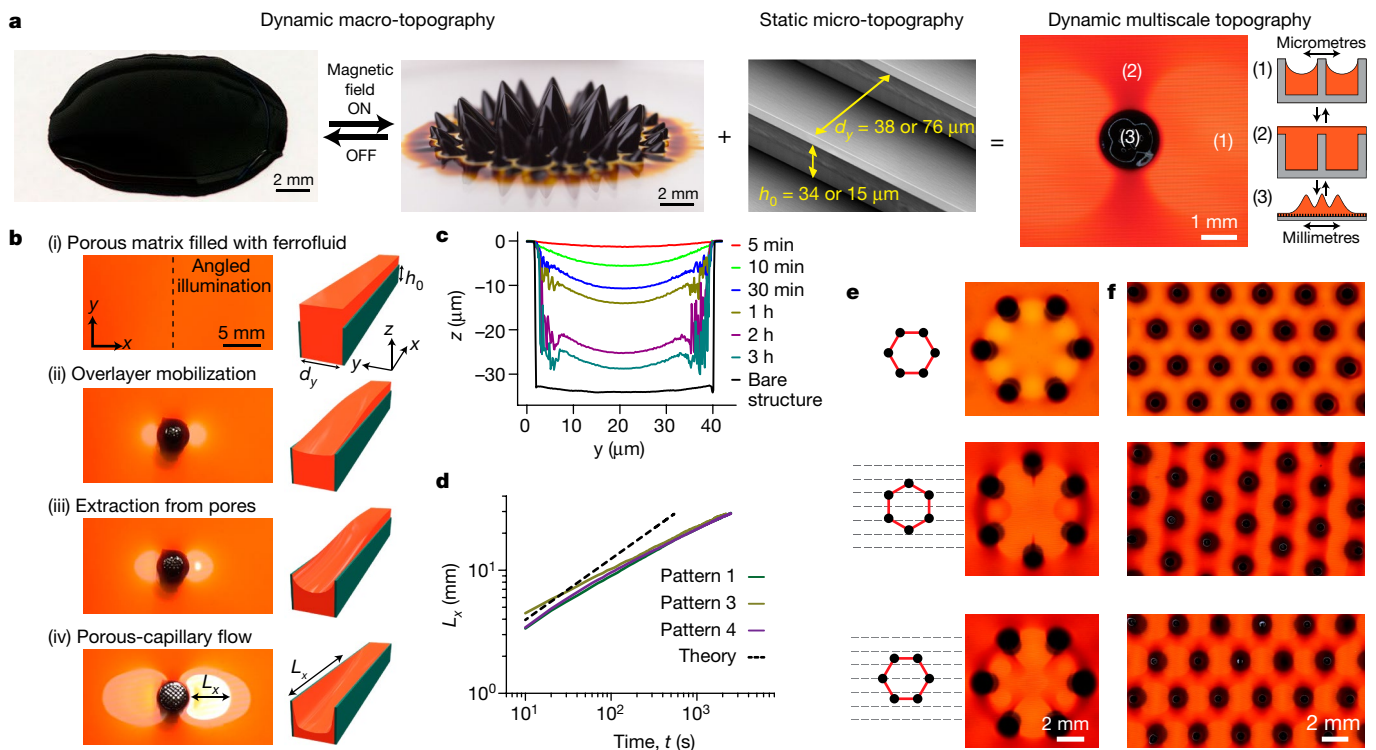
Fig. 1 | Dynamic multiscale topography of ferrofluid-containing liquid-infused porous surfaces (FLIPS). a, A diagram showing the concept of FLIPS. Left, two topographical states of a ferrofluid spreading on an unstructured surface, depicting the transformation from the flat interface to macroscale protuberances in response to an external magnetic field. Middle, scanning electron micrograph of the static micro-topography of exemplary microchannel substrates 1–3. Right, top-view photo of FLIPS under magnetic field, showing that the ferrofluid confined within the microstructured solid experiences area-selective topographical reconfigurations at multiple length scales: region (1) exhibits micro-topography shaped by the structured substrate; region (2) exhibits a flat surface; and region (3) exhibits the macro-topographical protuberance. **b**, Transport processes involved in the formation of macro- and micro-topographical features: the left column shows a series of representative experimental photos in top view, captured using the angled illumination technique; the right column shows the corresponding schematics, depicting the deformation of the ferrofluid–air interface in a microchannel. **c**, Evolution of cross-sectional profiles of the ferrofluid–air interface at a fixed distance (about 1.5 cm away from the magnet) over time, measured using a laser scanning microscope. **d**, Logarithmic plots of experimentally measured L_x versus time t for patterns 1, 3 and 4 from Table 1. The dashed black line is plotted using equation (2), with $\gamma = 17$ mN m^{-1}, $\eta = 0.367$ Pa s and $h_0 = 34$ μm. The overlayer thicknesses are ~10–20 μm. **e, f**, Snapshots of multiscale topographical response to a hexagonal pattern of six (**e**) or more (**f**) magnets (diameter, 1.6 mm; magnet spacing, 3.2 mm). The schematics on the left in **e** show the relative orientation of magnets with respect to microstructures. In **e** and **f**, the top row shows the case without a microstructured substrate; the bottom two rows show cases with the microstructured pattern 4, with different orientations of the hexagonal pattern.

where the speed of the advancing front is $U \approx \dot{L}_x$ and $\dot{L}_x = dL_x/dt$. Rearranging the terms and integrating with respect to time t gives a scaling relation for L_x:

$$L_x(t) \approx \left(\frac{\gamma h_0}{\eta}\right)^{1/2} t^{1/2} \quad (2)$$

where γ is the surface tension, η is the dynamic viscosity and h_0 is the height of the microstructure. The magnetic pressure $|p_m|$ generates a force on the ferrofluid, and an alternative derivation to the scaling relationship in equation (2) is obtained by replacing the left-hand side of equation (1) by the rate of change of work done by the magnet on the ferrofluid ($|p_m|\dot{L}_x d_y h_0$) and integrating with respect to time:

$$L_x(t) \approx \left(\frac{|p_m|h_0^2}{\eta}\right)^{1/2} t^{1/2} \quad (3)$$

Both derivations give the same power-law dependence with respect to time $L_x \propto t^{1/2}$, differing only in their pre-factors. Despite their simplicity, these scaling relations provide a reasonable order-of-magnitude approximation of the dynamics revealed in the experimental data. They also capture the dependence of L_x on h_0 and the independence of L_x from the spacing between micro-plates along the x direction d_x (see Extended Data Fig. 1a) and d_y. The discrepancy between the experiments and these scaling laws may be due to the three-dimensional shape of the microchannels, the complex shape of the ferrofluid–air interface and the dependence of L_x on the thickness of the ferrofluid overlayer (see Extended Data Fig. 2c), which the current models do not fully capture.

The asymmetry of the microchannels used in the demonstration above induces preferential asymmetric extraction of the ferrofluid from the channels along the x direction and the appearance of the characteristic dumbbell-shaped micro-topographical area (Supplementary Video 1). Additional length scales can be introduced by using patterned or structured magnetic fields applied to geometrically anisotropic FLIPS. Such fields can be created by organizing multiple permanent magnets into an array. For example, a hexagonal cluster of six magnets acting on a FLIPS with a channel-like array of microplates introduces one more symmetry element to the system, leading to more complicated flow patterns that reflect the relative orientation of the anisotropic microstructures in the patterned magnetic field (Fig. 1e). Because the field source is no longer axisymmetric, the orientation of the field source (six-fold rotational symmetry) with respect to the microplates (two-fold rotational symmetry) allows for one more degree of control over the topographical response (Fig. 1e, Supplementary Video 1), with the opportunity to expand the combination of symmetry elements in FLIPS to any combination of magnet assembly (for example, 'infinite' arrays of magnets; see Fig. 1f) and structured surface.

Table 1 | Structured surfaces used in this study

Pattern	Type	Dimensions (µm)
1	Array of microchannels	$d_x=0$, $d_y=38$, $h_0=34$
2	Array of microchannels	$d_x=0$, $d_y=38$, $h_0=15$
3	Array of microchannels	$d_x=0$, $d_y=76$, $h_0=34$
4	Array of microplates	$d_x=5$, $d_y=38$, $h_0=30$
5	Array of microposts	$d_x=1.4$, $d_y=1.4$, $h_0=10$
6	Spirally shaped channels	$d_x=0$, $d_y=38$, $h_0=15$
7	Microporous membrane	Average pore size = 1
8	Microporous membrane	Average pore size = 10
9	Microporous membrane	Average pore size = 20
10	Microporous tubing	Average pore size = 5–60

The FLIPS concept introduced here offers substantial versatility in designing dynamic surfaces with multiscale topographical responses. In the examples shown, we demonstrate that the specific topographical patterns can be finely tuned by controlling: (i) the properties of the ferrofluid (such as the type of magnetic particle, the concentration of magnetic particles, or the type and viscosity of the carrier fluid); (ii) the geometry of the microstructured substrate; (iii) the strength and pattern of the magnetic field; and (iv) the distance of the FLIPS from the magnets and their relative orientation. The resulting spatial and temporal dynamics of topographical reconfiguration enable numerous functions at multiple length scales.

At the micrometre scale, FLIPS provide a way of manipulating colloidal matter on two-dimensional interfaces (Fig. 2). Depending on the state of the dynamic topography, colloidal particles can form a disordered two-dimensional gas-like state (on flat topography; Fig. 2a) or organize into structures such as chains (on micro-topographical regions; Fig. 2b). Subsequently, FLIPS allow controlled transport of non-magnetic colloids when a horizontal body force on the ferrofluid is exerted by a lateral magnetic-field gradient (Fig. 2c, d). The transport mechanism is unique, because it does not correspond to either positive or negative magnetophoresis of magnetic colloidal matter, which have been studied extensively before[20]. Instead, the force on the non-magnetic particle is created by a hydrodynamic coupling of the ferrofluid flow under the field gradient to the motion of the aqueous phase on top of the ferrofluid (Fig. 2e). Under typical experimental conditions using small permanent magnets as field sources, the speed of the colloids is of the order of a few micrometres per second and controllable with the magnetic field (Fig. 2f, Supplementary Video 2).

Multiscale topography can also be used to assemble colloidal matter into otherwise inaccessible hierarchical structures. For example, in the case of ferrofluid-coated unstructured surfaces, a hexagonal, soft, ferromagnetic nickel grid leads to the formation of a hexagonally varying, periodic ferrofluid pattern on which colloidal particles assemble into close-packed clusters (Fig. 2g); in the case of FLIPS, a multiscale topographical response is created, and colloidal matter additionally organizes into short line segments as dictated by the two symmetries (Fig. 2h).

At the millimetre scale, FLIPS can be harnessed for controlling the motion, clustering and interaction of liquid droplets. We use gravity
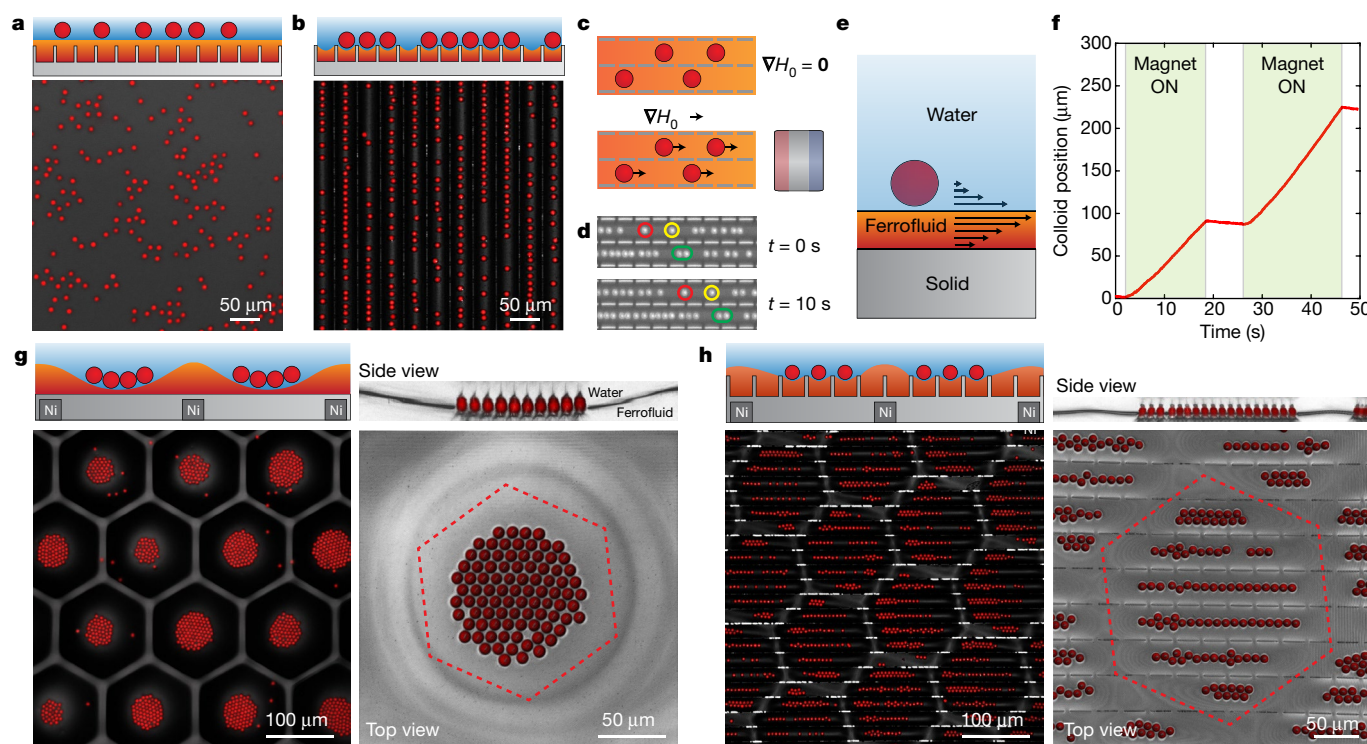

Fig. 2 | Manipulation of non-magnetic colloidal particles on FLIPS (application of FLIPS at micrometre scale). a, b, Schematics (top) and confocal fluorescence images (bottom) of 10-µm-diameter melamine colloidal particles floating on the flat surface of FLIPS in the absence of a magnetic field (**a**) and confined in micro-topography of FLIPS when the ferrofluid has been locally depleted from the microstructures using a magnet (**b**). **c,** Schematics showing colloidal particles staying stationary in the absence of a magnetic-field gradient ($\nabla H_0 = 0$; top) and moving in the presence of a magnetic-field gradient that is created by a magnet on the right (direction of ∇H_0 indicated by the arrow; bottom). **d,** Optical images showing the transport of colloidal particles along the micro-topographical region. Four particles are labelled to depict their movement within a 10s interval. **e,** Schematic illustrating the mechanism behind the transport of non-magnetic colloidal particles in a magnetic field: the transport of ferrofluid induces a flow of the water near the ferrofluid–water interface, leading to the transport of the colloidal particles. **f,** Plot of relative colloidal positions along the channels as a function of time; the green shaded areas indicate the times when the magnet field is turned on. **g, h,** Schematics (top left) and confocal fluorescence (side views on the top right and top views at the bottom) images showing the confinement of colloidal particles by the macro-topographical response of a thin layer of ferrofluid alone (without micro-topography; **g**) and the confinement of colloidal particles by the macro- and micro-topographical response of FLIPS (**h**). A hexagonal nickel grid embedded in FLIPS is used to shape a nearly uniform external magnetic field into a hexagonally varying field-intensity pattern. Schematics are not shown to scale.
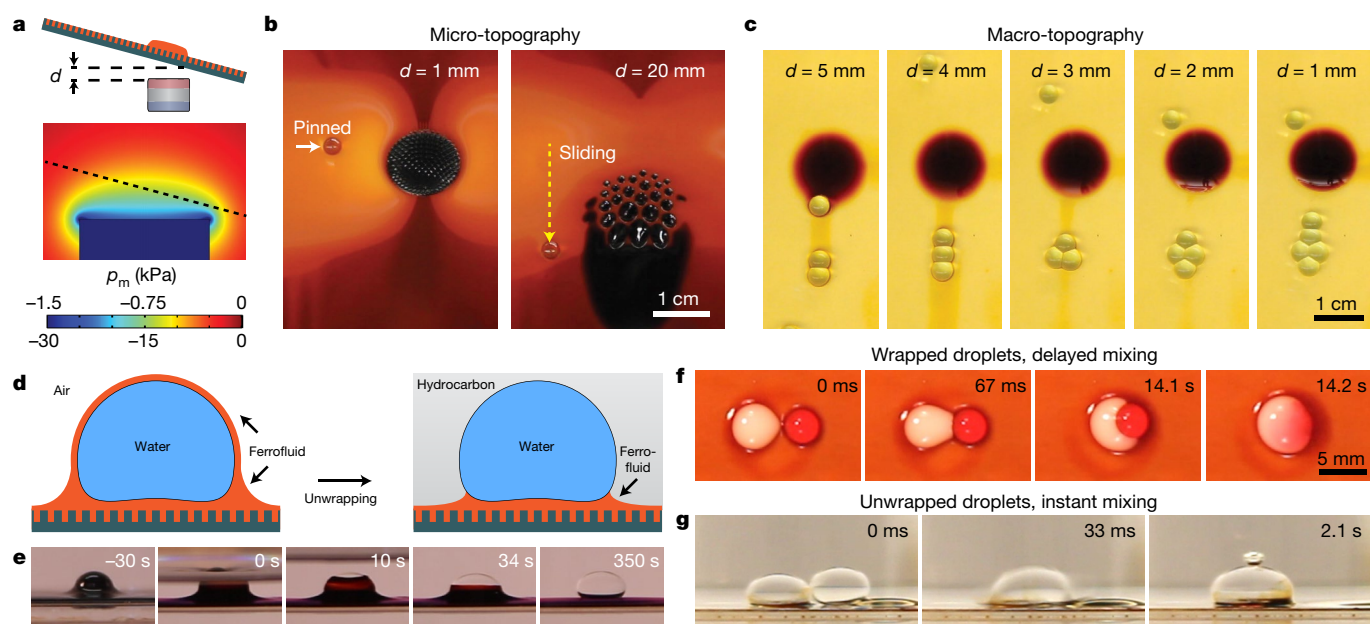
Fig. 3 | Control of droplet flow and droplet manipulation (application of FLIPS at millimetre scale). a, Top, schematic showing the configuration of the experimental set-up in **b** and **c**. The FLIPS is tilted and placed at a distance d above the magnet. Bottom, simulated magnetic pressure distribution (p_m) around the magnet. The upper and lower scales of the colour scale correspond to **c** and **b**, respectively. **b**, Two photographs showing a water droplet pinned on the micro-topographical area and its subsequent release after the magnet is lowered to allow ferrofluid to flow back and submerge the micro-topography. **c**, Five photographs showing different clustering behaviours of 15-μl water droplets on the macro-topographical feature at five different distances d. This FLIPS used diluted ferrofluid and hence did not have a micro-topographical area. **d**, Schematic showing the unwrapping of a thin ferrofluid layer around a water droplet by changing the surrounding medium from air to a hydrocarbon liquid. **e**, Five photographs showing the unwrapping of a thin layer of ferrofluid around a water droplet after the addition of dodecane. **f**, Four photographs showing the delayed mixing of two liquid droplets in the presence of wrapping layers. The white and red droplets are the suspension of 10-μm-diameter polystyrene colloids in ethanol–water mixture and in water dyed with rhodamine B, respectively. They were brought together by a stationary alternating-current electromagnet at the centre beneath the FLIPS. **g**, Three photographs showing instant mixing of two droplets in the absence of wrapping layers. The left droplet is an aqueous solution of sodium bicarbonate and the right droplet is an aqueous solution of 2 M hydrochloric acid. The right image shows the CO_2 bubble formed after the coalescence of the droplets.

to drive the flow of droplets on a tilted FLIPS, and tune the multiscale topographical response by adjusting the magnetic-field strength and gradients by varying the distance d between the magnet and FLIPS (Fig. 3a). On the one hand, the reversible appearance of micro-topography creates switchable slippery surfaces[21] that pin the droplets at micro-topographical regions or release the droplets when the magnetic-field strength is reduced to remove the micro-topography (Fig. 3b, Supplementary Video 3). On the other hand, the macro-topographical protuberance can be used to assemble droplets into well-defined clusters (Fig. 3c). To demonstrate this behaviour, we note that when a droplet slides near the protuberance it is pinned to it by capillary and magnetic forces. Subsequent droplets will enter the trap and combine with the previously pinned droplets to form clusters, until their collective gravity overcomes their attraction to the protuberance. They are then released as doublets, triplets, quadruplets or quintuplets, depending on the adhesion that is controlled by the distance between the magnet and the FLIPS (Supplementary Video 4). If the droplets contain polymerizable moieties, then these clusters can be solidified into distinct assemblies.

Another droplet-manipulation strategy involves control over the formation of the ferrofluid wrapping layer around the droplets. For example, by replacing air with an alternative liquid medium that is immiscible with the ferrofluid or the droplets, such as a hydrocarbon, the non-transparent ferrofluid wrapping layer around the water droplets can be removed (Fig. 3e, Supplementary Video 5). This unwrapping can be used to accelerate the coalescence of droplets: compared to the wrapped droplets, for which the mixing is delayed by more than 10 s (Fig. 3f), the unwrapped droplets mix instantaneously (Fig. 3g, Supplementary Video 6), enabling rapid initiation of chemical reactions. Although existing theory suggests that the formation of a wrapping layer is due to a positive spreading coefficient[12,22], we found that

long-range van der Waals interaction is likely to be the decisive force in determining the presence or absence of the wrapping layers; see detailed discussion in Methods section 'Additional notes on the formation of the wrapping layer', Extended Data Tables 1–4 and Extended Data Figs. 4 and 5[23–26].

Finally, we illustrate the versatility of FLIPS at the centimetre scale by demonstrating switchable adhesion and friction, liquid pumping and biofilm removal. We measure the adhesion between FLIPS and other surfaces by first pressing the test surface against the FLIPS and then lifting them. With the magnetic field on, deforming the macroscopic protuberances and driving the ferrofluid back into the porous matrix requires external work. Conversely, from an energetic viewpoint, the formation of the macroscopic protuberance is favoured and can spontaneously open a gap between the FLIPS and the test surface, which enables switchable adhesion (Fig. 4a, Supplementary Video 7, Extended Data Fig. 6a–c) and friction (Supplementary Video 8). Notably, in contrast to traditional ferrofluid-coated unstructured surfaces, FLIPS display area-specific adhesion and friction: regions with flat ferrofluid, with macrostructured protuberances, and with micro-topography, have characteristically different values (Extended Data Fig. 6d–h). Furthermore, the anisotropic geometry and arrangement of the microstructures introduce directionality to friction that can be controlled magnetically (Extended Data Fig. 6i) to create tunable anisotropic-friction materials.

By coupling the ability of the magnets to extract ferrofluid from microporous structures and the movement of the magnets, we demonstrate pumping liquids at the centimetre scale (Fig. 4b, Supplementary Video 9). We infuse a porous polytetrafluoroethylene (PTFE) tube with ferrofluid to form a FLIPS pipe. A stepper motor moves five pairs of magnets in a circular motion. The ferrofluid between each pair of magnets moves as the magnets rotate and pushes the test liquid along the tube. The porosity of the PTFE tube wall allows the ferrofluid to
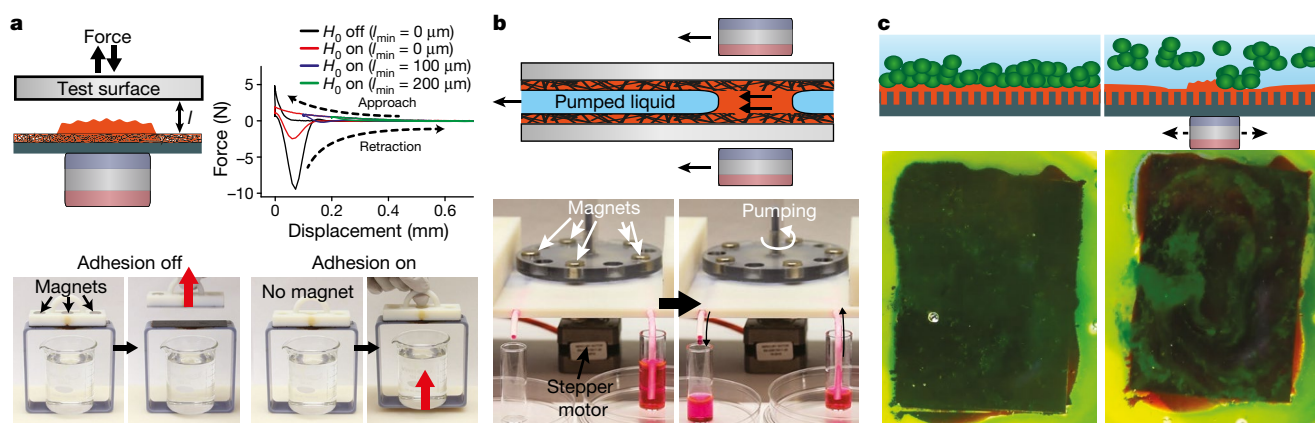
Fig. 4 | Adhesion, pumping and biofilm removal (application of FLIPS at centimetre scale). a, Adhesion. The top left schematic shows the set-up for adhesion measurement. The test surface is brought in contact with FLIPS at a speed of 0.1 mm s^{-1}, held still for 10 s and then lifted at 1 mm s^{-1}. An example of the resulting force–distance curve is shown at top right. The test surface in this example is a smooth PTFE. The photographs at the bottom demonstrate switchable adhesion. **b**, Pumping. The top

is a schematic of the pumping mechanism. The pair of magnets moves the ferrofluid plug along the FLIPS pipe, which in turn drives the liquid (blue) flow inside the pipe. The bottom photographs show that an ethanol solution of rhodamine B is pumped from the right vial to the left vial. **c**, A green algae biofilm is removed by swirling a magnet under FLIPS. Note that the ferrofluids used in these experiments are not toxic, as indicated by the green colour of the algal biofilm.

follow the circular motion of the pairs of magnets, resulting in continuous pumping enabled by a simple rotation, without the need for any complex sequential movement of magnets, as described previously[27]. Last, using a non-toxic fluorocarbon-based ferrofluid, we demonstrate biofilm removal from FLIPS (Fig. 4c). We cultured the algae biofilm on FLIPS under quiescent conditions for about a week, and then moved a magnet under the FLIPS and used the macroscopic protuberance to disrupt the green algae biofilm and detach it from the surface (Supplementary Video 10).

The multiscale topographical response of FLIPS not only has intriguing spatial and temporal fluid dynamics features, but also provides a wide range of interesting phenomena and novel functions when interfaced with other solids and liquids. Our results suggest that FLIPS allows much more diverse combinations of functional capabilities than surfaces that have only a simple, single-scale topographical response. The applications that we have demonstrated—new forms of hierarchical colloidal self-assembly, manipulation and transport of non-magnetic matter in a magnetic field enabled by topography-induced hydrodynamic and capillary forces, controlled formation of droplet clusters of well-defined size, and switchable and directional adhesion and friction—are a small representative subset of these capabilities. Nonetheless, this subset goes well beyond recently reported examples of manipulation of magnetic droplets, controlled wettability and slippery ice-phobic surfaces[5,12–14,18,21,27]. We emphasize the customizability of topographical reconfigurations of FLIPS, which can be tuned by changing the magnetic field, the ferrofluid and, especially, the geometry and orientation of the confining microstructured surface, which itself can be made dynamic by using flexible microstructures[9,28]. The mechanistic insights gained in understanding the physical forces that govern these phenomena and the ensuing functions can be readily applied to other technologically relevant developments: for example, to explore the influence of surface topography on turbulent flow[29], to explore the use of the magneto-caloric effect[15] to manage heat transfer with its surrounding system[30], and to explore the minimization of the pump for novel microfluidics platforms[31]. In addition, we expect the concept of dynamically reconfigurable multiscale topographies to find uses in biology, such as for controlling and stimulating living matter simultaneously at multiple length scales[32–34]. We anticipate that FLIPS and their future developments will benefit areas such as responsive coatings, digital microfluidics and the interfacing of biological tissues with dynamic materials.

Online content

Any Methods, including any statements of data availability and Nature Research reporting summaries, along with any additional references and Source Data files, are available in the online version of the paper at https://doi.org/10.1038/s41586-018-0250-8.

1. Vaia, R. & Baur, J. Adaptive composites. *Science* **319**, 420–421 (2008).
2. Kuroki, H., Tokarev, I. & Minko, S. Responsive surfaces for life science applications. *Annu. Rev. Mater. Res.* **42**, 343–372 (2012).
3. Xia, F. & Jiang, L. Bio-inspired, smart, multiscale interfacial materials. *Adv. Mater.* **20**, 2842–2858 (2008).
4. Yoshida, R. Self-oscillating gels driven by the Belousov–Zhabotinsky reaction as novel smart materials. *Adv. Mater.* **22**, 3463–3483 (2010).
5. Reddy, S., Arzt, E. & del Campo, A. Bioinspired surfaces with switchable adhesion. *Adv. Mater.* **19**, 3833–3837 (2007).
6. van Oosten, C. L., Bastiaansen, C. W. M. & Broer, D. J. Printed artificial cilia from liquid-crystal network actuators modularly driven by light. *Nat. Mater.* **8**, 677–682 (2009).
7. Liu, D., Liu, L., Onck, P. R. & Broer, D. J. Reverse switching of surface roughness in a self-organized polydomain liquid crystal coating. *Proc. Natl Acad. Sci. USA* **112**, 3880–3885 (2015).
8. Liu, D. & Broer, D. J. New insights into photoactivated volume generation boost surface morphing in liquid crystal coatings. *Nat. Commun.* **6**, 8334 (2015).
9. Sidorenko, A., Krupenkin, T., Taylor, A., Fratzl, P. & Aizenberg, J. Reversible switching of hydrogel-actuated nanostructures into complex micropatterns. *Science* **315**, 487–490 (2007).
10. He, X. M. et al. Synthetic homeostatic materials with chemo-mechano-chemical self-regulation. *Nature* **487**, 214–218 (2012).
11. Aizenberg, J., Hatton, B., Yao, X., Aizenberg, M. & Wang, W. Dynamic and switchable slippery surfaces. US patent 9,683,197 (2017).
12. Khalil, K. S., Mahmoudi, S. R., Abu-dheir, N. & Varanasi, K. K. Active surfaces: Ferrofluid-impregnated surfaces for active manipulation of droplets. *Appl. Phys. Lett.* **105**, 0416604 (2014).
13. Tian, D. et al. Fast responsive and controllable liquid transport on a magnetic fluid/nanoarray composite interface. *ACS Nano* **10**, 6220–6226 (2016).
14. Irajizad, P., Hasnain, M., Farokhnia, N., Sajadi, S. M. & Ghasemi, H. Magnetic slippery extreme icephobic surfaces. *Nat. Commun.* **7**, 13395 (2016).
15. Rosensweig, R. E. *Ferrohydrodynamics* (Dover Publications, Mineola, 1997).
16. Rosensweig, R. E. Magnetic Fluids. *Sci. Am.* **247**, 136–145 (1982).
17. Odenbach, S. (ed) *Lecture Notes in Physics: Colloidal Magnetic Fluids: Basics, Development and Application of Ferrofluids* (Springer, Berlin, 2009).
18. Timonen, J. V. I., Latikka, M., Leibler, L., Ras, R. H. A. & Ikkala, O. Switchable static and dynamic self-assembly of magnetic droplets on superhydrophobic surfaces. *Science* **341**, 253–257 (2013).
19. Torres-Díaz, I. & Rinaldi, C. Recent progress in ferrofluids research: novel applications of magnetically controllable and tunable fluids. *Soft Matter* **10**, 8584–8602 (2014).
20. Timonen, J. V. I., Demirörs, A. F. & Grzybowski, B. A. Magnetofluidic tweezing of nonmagnetic colloids. *Adv. Mater.* **28**, 3453–3459 (2016).
21. Yao, X. et al. Adaptive fluid-infused porous films with tunable transparency and wettability. *Nat. Mater.* **12**, 529–534 (2013).
22. Schellenberger, F. et al. Direct observation of drops on slippery lubricant-infused surfaces. *Soft Matter* **11**, 7617–7626 (2015).
23. Parsegian, V. A. *Van der Waals Forces: a Handbook for Biologists, Chemists, Engineers, and Physicists* (Cambridge Univ. Press, Cambridge, 2006).
24. Israelachvili, J. N. *Intermolecular and Surface Forces* 3rd edn, Ch. 13 (Academic Press, Burlington, 2011).
25. Reiter, G. et al. Thin film instability induced by long-range forces. *Langmuir* **15**, 2551–2558 (1999).

26. Daniel, D., Timonen, J. V. I., Li, R., Velling, S. J. & Aizenberg, J. Oleoplaning droplets on lubricated surfaces. *Nat. Phys.* **13**, 1020–1025 (2017).
27. Hatch, A., Kamholz, A. E., Holman, G., Yager, P. & Bohringer, K. F. A ferrofluidic magnetic micropump. *J. Microelectromech. Syst.* **10**, 215–221 (2001).
28. Grinthal, A. & Aizenberg, J. Adaptive all the way down: building responsive materials from hierarchies of chemomechanical feedback. *Chem. Soc. Rev.* **42**, 7072–7085 (2013).
29. McKeon, B. J., Sharma, A. S. & Jacobi, I. Experimental manipulation of wall turbulence: A systems approach. *Phys. Fluids* **25**, 031301 (2013).
30. Park, K.-C. et al. Condensation on slippery asymmetric bumps. *Nature* **531**, 78–82 (2016).
31. Pamme, N. Magnetism and microfluidics. *Lab Chip* **6**, 24–38 (2006).
32. Verho, T. et al. Reversible switching between superhydrophobic states on a hierarchically structured surface. *Proc. Natl Acad. Sci. USA* **109**, 10210–10213 (2012).
33. Epstein, A. K., Wong, T. S., Belisle, R. A., Boggs, E. M. & Aizenberg, J. Liquid-infused structured surfaces with exceptional anti-biofouling performance. *Proc. Natl Acad. Sci. USA* **109**, 13182–13187 (2012).
34. Sutton, A. et al. Photothermally triggered actuation of hybrid materials as a new platform for *in vitro* cell manipulation. *Nat. Commun.* **8**, 14700 (2017).

Author contributions J.A., W.W. and J.V.I.T. designed the experiments. W.W. performed the experiments on the dynamics of micro-topography, droplet manipulation, pumping and wrapping-layer-related calculations. J.V.I.T. performed experiments with magnet arrays and manipulation of colloids. C.T.Z. fabricated the microstructures. D.-M.D. measured the ferrofluid overlayer thickness. D.-M.D., M.S. and W.W. performed the adhesion and friction measurements. S.Ko. and J.V.I.T. performed the biofilm experiments. L.M., A.C., W.W. and J.V.I.T. performed the scaling analysis. A.G. assisted in the design of experiments. S.Ke. and J.C. assisted in droplet experiments. R.T.B. assisted in the pump design. T.-S.W., B.H. and S.H.K. contributed to the initial conception of the project. J.A., W.W., J.V.I.T., A.G. and A.C. wrote the manuscript. J.A. supervised the research.

Competing interests The authors declare no competing interests.

Additional information
Extended data is available for this paper at https://doi.org/10.1038/s41586-018-0250-8.
Supplementary information is available for this paper at https://doi.org/10.1038/s41586-018-0250-8.
Reprints and permissions information is available at http://www.nature.com/reprints.
Correspondence and requests for materials should be addressed to J.A.
Publisher's note: Springer Nature remains neutral with regard to jurisdictional claims in published maps and institutional affiliations.

METHODS

Materials. Hexamethyldisiloxane (HMDS) was obtained from Microchem. Positive i-line photoresist megaposit SPR700-1.0 and developer microposit MF CD-26 were obtained from Microchem. Trichloro(1H,1H,2H,2H-perfluorooctyl) silane (13F-silane) was obtained from Sigma-Alrich. Sylgard 184 silicone (PDMS) elastomer kit was obtained from Dow Corning. Ultraviolet (UV)-curable epoxies (EPO-TEK OG142 and OG178) were obtained from Epoxy Technology. Polytetrafluoroethylene (PTFE) membranes with average pore sizes of $1\,\mu m$, $10\,\mu m$ or $20\,\mu m$ were obtained from Sterlitech and used as received. Aeos extruded microporous ePTFE tubing (ID 0.0775″ and wall thickness 0.034″, internodal distance $5–60\,\mu m$) was obtained from Zeus and used as received. Neodymium magnets (surface fields 1,000–5,000 G) were obtained from K&J magnets or Supermagnete. Alnico magnets were obtained from All Magnetics. Fluorocarbon-based ferrofluids were obtained from Ferrotec. The perfluoropolyether oil used in the dilution of ferrofluids was Dupont Krytox 100, obtained from 3 M. Extended Data Table 1a summarizes the physical properties of the two types of fluorocarbon-based ferrofluid used in our experiments as well as the properties of Krytox 100. Reagent plus grade dodecane was obtained from Sigma-Aldrich.

The silicone-oil-based ferrofluid was synthesized by using the coprecipitation method. In brief, 720 ml of milli-Q water was mixed with 21.6 g of iron(III) chloride hexahydrate and 11.2 g of iron(II) sulfate heptahydrate, followed by coprecipitation by adding 80 ml of ammonium hydroxide (28%–30%). The iron oxide nanoparticles formed were functionalized by adding 25 g of monocarboxydecyl-terminated polydimethylsiloxane (Gelest MCR-B12) and allowing it to react overnight. Particles were purified by sedimenting them with a strong magnet, followed by removal of the aqueous supernatant and adding 400 ml of acetone to redisperse the particles. Particles were further magnetically sedimented, acetone supernatant discarded, and 250 ml of toluene added. Particles were again magnetically sedimented and toluene supernatant removed. Finally, 50 ml of toluene was added and any remaining traces of acetone were removed by heating to 60 °C for a few hours. The resulting volume of the ferrofluid in toluene was approximately 80 ml. Finally, iron oxide particles were transferred to silicone oil by mixing the nanoparticle dispersion in toluene with silicone oil and evaporating the toluene. Fluorocarbon-based and silicone-oil-based ferrofluids provide qualitatively similar results.

The preparations of different FLIPS and additional materials for specific experiments are described in detail below.

Microstructured substrates. Microstructured silicon substrates (masters) were fabricated using the Bosch process and replicated using soft lithography based on previous protocols[35,36]. In brief, adhesion promoter (HMDS) and positive i-line photoresist (SPR700-1.0, about $2\,\mu m$ height) were spin-coated onto a clean wafer, soft-baked at 95 °C for 60 s, patterned using a direct write laser tool (Heidelberg, Maskless Aligner, 405 nm laser at about 125 mJ cm^{-2} s^{-1}), hardened at 115 °C for 60 s, and developed in the developer CD-26 for around 90 s. The photoresist-patterned silicon wafer was then ion-etched under optimized Bosch conditions (SPTS Technologies) to nominal height and rinsed in acetone/isopropanol to remove residual photoresist. The resulting silicon microstructures were treated with plasma and passivated with 13F-silane under vacuum for more than 6 h. The silicon masters were then used to prepare polydimethylsiloxane (PDMS) negative moulds. PDMS prepolymer (base-to-hardener ratio of 10:1, wt/wt) was poured onto the master, cured at 70 °C for 2 h, and peeled from the masters to obtain negative moulds. PDMS negative moulds were stored in 13F-silane vapour environment for more than 3 h. The PDMS moulds were then used to create an epoxy positive replica. A few millilitres of epoxy (EPO-TEK OG142 or OG178) were cast at the centre of a Petri dish using a plastic pipette. A PDMS mould was then carefully placed over the epoxy to prevent bubbles from forming between PDMS and the epoxy layer. To obtain epoxy replicas with areas smaller than that of the PDMS moulds, a few drops of epoxy (less than 1 ml) were cast on PDMS mould, and a clean glass slide (rinsed with acetone, isopropanol and water, and blow-dried with nitrogen) was placed slowly over the epoxy, followed by curing under UV light (Bio-Link 365, Vilber) for 20 min. The PDMS mould was then peeled off slowly to give the microstructured positive epoxy replica. Any variations of the procedures for preparing positive epoxy replicas are described in the relevant sections.

Dynamics of the micro-topographical response of FLIPS. The silicon masters are prepared on 10-cm wafers (area of about 80 cm^2). Epoxy replicas were made inside a 13.5-cm-diameter Petri dish. To prepare FLIPS, 0.4 ml of fluorocarbon-based ferrofluid 1 was dropped onto the epoxy microstructures and spread over the substrate surface with a magnet. To vary the overlayer thickness, the FLIPS sample was spun at 500 r.p.m. for a period of 1–5 min, and the overlayer thickness was measured directly using a force probe (see below). At the beginning of each experiment, magnets were fixed to the back of the Petri dish using double-sided tape. For the data presented in Fig. 1d and Extended Data Fig. 2c, a 10-mm-diameter and 40-mm-tall N45 neodymium iron boron (NdFeB) magnet was used. In other control experiments, 0.5-inch-diameter and 0.5-inch-tall N52 NdFeB or 4-mm-diameter and 7-mm-tall N45 NdFeB was used. The dynamics of the micro-topographical

response was recorded using an angled illumination technique (see below). The videos were then analysed using a custom Matlab code. The colour thresholding was performed on V values in the HSV colour space. In the experiments with the spiral pattern, 4-mm-diameter and 7-mm-tall N45 NdFeB was used.

Angled illumination technique (Extended Data Fig. 1b). A cold LED line light (Zeiss CL 6000) was used to illuminate the FLIPS sample at an incidence angle of approximately 30°. A video camera (Sony HDR CX900) was positioned directly above the FLIPS sample to record the process. Scattered light from the micro-topographical regions greatly increased the brightness of the region and facilitated the video-processing step of the analysis.

Force-probe technique to measure the thickness of the ferrofluid overlayer (Extended Data Fig. 1c). A spherical glass probe was lowered on the FLIPS surface at a controlled speed of $10\,\mu m$ s^{-1}. Force was recorded at 1-ms intervals using a load cell (Transducer Techniques). The probe was programmed to stop when a contact force of 50 mN was reached. The thickness of the ferrofluid overlayer was then determined from the resulting force–displacement curve as the distance between capillary snap-in and the position where the probe touches the top of the microstructure.

Measurement of 3D profiles of the ferrofluid–air interface. The 3D profiles of the ferrofluid–air interface were measured using a 3D laser-scanning confocal microscope (Keyence) with a 100× long-working-distance objective. For the data on the evolution of 3D profiles over time and the change in profiles along the x axis (Fig. 1c, Extended Data Fig. 2), the microstructured substrates used were epoxy replicas of pattern 1 fabricated on a 1 inch × 3 inch glass slide, with the microchannels aligned parallel to the long edge of the glass slide, and fluorocarbon-based ferrofluid 1 was used. A 4-mm-diameter and 7-mm-tall N45 NbFeB magnet was used. For the data on fine-tuning the balance between magnetic and capillary pressures (Extended Data Fig. 3), the microstructured substrates were epoxy replicas of pattern 1 fabricated on a 1 inch × 3 inch glass slide, with the microchannels aligned perpendicular to the long edge of the glass slide, or epoxy replicas of pattern 5. Fluorocarbon-based ferrofluid 1 was used. The magnets used were either 10-mm-diameter and 7-mm-tall N45 NdFeB magnets or 0.5-inch-diameter and 0.5-inch-tall Alnico magnets with a surface field of 0.041 T.

Topographical responses to magnet arrays. FLIPS were prepared with epoxy replicas of pattern 4 on a 1-mm-thick glass slide. Fluorocarbon-based ferrofluid 1 was used to induce both micro-topographical and macro-topographical responses. Multiple small cylindrical magnets were first embedded into an acrylic sheet. The sheet was drilled with a hexagonal pattern of circular holes with a CO$_2$ laser-cutting system (Versalaser). The diameter of the holes was chosen to be slightly less than the diameter of the cylindrical magnets (K&J Magnetics, NdFeB, diameter 1/16″) so that individual magnets could be mounted by simply pressing them into the holes without using any adhesives. The magnet array was placed on top of a white-LED panel light and the FLIPS was lowered on top of the magnet array (to direct contact with the magnets). The propagation of the depletion pattern was imaged immediately with a digital camera (Panasonic DMC-GH4) equipped with a macro lens (Olympus Zuiko 60 mm).

Applications in colloidal assembly and transport. *Assembly of non-magnetic colloidal particles on FLIPS.* The microplate array (pattern 4) was created on the top of a standard 1 inch × 3 inch glass slide by replication moulding of a silicon master. In brief, PDMS (1:10) was cast on the silicon master, degassed under vacuum, cured at 70 °C and peeled off. The resulting negative mould was filled with UV-curable photopolymer (Norland Optical Adhesive 61) and pressed against the glass slide. Photopolymer was cured under UV light (Dymax 2000-EC) for about 1 min and the PDMS mould was peeled off. A liquid reservoir for the colloidal dispersion was created by attaching an aluminium washer ring (inner diameter of about 20 mm, height of a few millimetres) on top of the microstructures with the same UV-curable photopolymer. The microstructures were then lubricated by adding a droplet of non-diluted fluorocarbon-based ferrofluid (Ferrotec) or silicone-oil-based ferrofluid to completely cover the microplates. After the microplates were covered with ferrofluid, the ferrofluid could be locally depleted from the microstructures by applying a local magnetic field with a small permanent magnet. The reservoir was filled with a colloidal dispersion consisting of non-magnetic carboxylate-modified fluorescent (rhodamine-B-marked) melamine microparticles $10\,\mu m$ in diameter (Sigma-Aldrich). Colloidal particles were allowed to settle down for a few hours after which they were imaged with an upright confocal microscope (Zeiss LSM710) with water-dipping objectives (40×/1.0 and 10×/0.3). Depending on the state of the FLIPS surface, the colloids were found to assemble randomly on the 2D plane (flat ferrofluid–water interface; Fig. 2a) or to follow the underlying microstructure, forming particle chains (partially depleted structures in micro-topographical area; Fig. 2b).

Hierarchical assembly. More complicated colloidal assemblies were created by using magnetically patterned FLIPS surfaces. The FLIPS substrates were created in the same way as described in Methods subsection 'Assembly of non-magnetic colloidal particles on FLIPS', with the exception that a hexagonal nickel grid

(Gilder hexagonal grid 100 mesh, Ted Pella) was placed between the glass slide and the PDMS mould filled with photopolymer before curing it with UV light, resulting in a microplate array with a magnetic grid under it (Fig. 2h). If no microplates were desired (that is, plain flat surface), then a flat PDMS block was used (Fig. 2g). Lubrication and colloidal assembly were carried out as described in the previous section.

Transport of non-magnetic colloids on FLIPS. Magnetically induced motion of the non-magnetic colloids was demonstrated by applying a horizontal magnetic-field gradient on the colloids that had settled on a partially depleted micro-topographical area of FLIPS. A gradient was created by placing an NdFeB magnet (cube, about 1-inch sides) next to the substrate and imaging was done with a long-working-distance zoom microscope (Zeiss AxioZoom). Motion of the colloids was stopped by removing the magnet (Fig. 2c–f).

Droplet flow control. *Effect of micro-topography.* FLIPSs were prepared with microstructured epoxy replicas of pattern 4 for the first part of the demonstration and of pattern 1 for the second part of the demonstration. For the second part of the demonstration, the angled illumination technique was used to visualize the micro-topographical region directly. Fluorocarbon-based ferrofluid 1 was used to induce a micro-topographical response. FLIPS was placed at a tilt angle of 15°–30° to induce droplet flow due to gravity. A stack of permanent magnets (three to four 0.5-inch-diameter and 0.5-inch-tall N52 NdFeB for the first demonstration; five 4-mm-diameter and 7-mm-tall NdFeB for the second demonstration) was placed on the top of a linear actuator (Firgelli L12P Linear Actuator w/ LAC); the use of a stack of magnets helps to extend the magnetic field along the z direction. The linear actuator has an actuation range of 10 cm and was used to adjust the relative vertical position of the magnets with respect to FLIPS precisely. During an experiment, the magnets were first brought close to FLIPS, with a separation distance of about 1 mm, to induce a micro-topographical response. After the micro-topographical region was formed, usually after about 30 min, a droplet of water (5–10 μl) was placed in the area above the micro-topographical region so that it would begin to slide down owing to gravity. Once the droplet moved into the micro-topographical region, it slowed and eventually stopped. The magnets were lowered to a distance 10–20 mm below the FLIPS so that the ferrofluid could flow back to the micro-topographical region, allowing the droplet to begin sliding again.

Effect of macro-topography. FLIPSs were prepared with microstructured epoxy replicas of pattern 4. Fluorocarbon-based ferrofluid 2 was diluted to 4% by volume with Krytox 100 to reduce the magnetic pressure and suppress the micro-topographical response. A stack of permanent magnets (three to four 0.5-inch-diameter and 0.5-inch-tall N52 NdFeB) was placed on the top of a linear actuator (Firgelli L12P Linear Actuator w/ LAC). The linear actuator has an actuation range of 10 cm and was used to adjust the relative vertical position of the magnets with respect to FLIPS precisely. Furthermore, the linear actuator was attached to a translational stage that was adapted and modified from the x-stage of the 3D printer RepRapPro Huxley. The x-stage and the linear actuator were both controlled through a PC interface. In the experiment, the magnets were first brought close to the FLIPS, with a separation distance of about 1 mm, to form the macro-topographical protuberance. A syringe equipped with a needle, pumped by a syringe pump, was positioned at the top of the FLIPS to introduce a flow of droplets. The magnets were then translated in the horizontal direction to move the macroscopic protuberance into the track of the droplet flow to induce droplet pinning. The magnets were then lowered successively to the desired distance from FLIPS (1–5 mm) to induce different assembling behaviours of droplets.

Control of the wrapping layer formation and droplet mixing. *Interfacial tension measurements.* Surface and interfacial tension measurements of various liquids used in the study were performed on KSV Instruments's CAM 101 system using the pendant drop method. Deionized water with a resistivity of more than 18.2 MΩ cm was collected from Millipore's Milli-Q water system. Dodecane of analytical standard grade (AS, >99.8%) and reagent plus grade (RP, >99%) were obtained from Sigma-Aldrich; dodecane of 99+% grade was obtained from Alfa Aesar.

Formation and removal of wrapping layers. FLIPS were prepared with porous PTFE membranes with 1-μm pore size to suppress the micro-topographical response. Fluorocarbon-based ferrofluids and their 4%-by-volume dilution by the fluorocarbon oil Krytox 100 were used in the experiments to study the wrapping layer, to avoid mixing between the ferrofluid and the content of the droplets. For the experiments shown in the Supplementary Video 5, ferrofluid 2 was used. A camera (Cannon Repel T2i) was used to record the experiment. For the formation of the wrapping layer, a water droplet was placed slowly on the FLIPS in air. For the removal of the wrapping layer, the FLIPS and the water droplet were placed in a beaker, into which a hydrocarbon was added slowly.

Mixing droplets with wrapping layers. FLIPS were prepared on porous PTFE membranes with 1-μm pore size to suppress the micro-topographical response. Fluorocarbon-based ferrofluid 2 diluted to 4% by volume with Krytox 100 was used. The electromagnet in this experiment consisted of 286 turns of a heavy film #14 AWG wire wrapped around a 2.61-cm-long and 0.9-cm-diameter iron-cobalt-vanadium Hiperco 50 alloy core (custom fabrication from Dura Magnetics). This electromagnet was designed to operate between 1 Hz and 550 Hz, producing non-hysteretic sinusoidal magnetic fields of more than 0.2 T when powered using an APS-1102 programmable AC/DC power source (Instek America). In the experiment, two droplets of colloidal suspensions (10 μl each) were placed near the centre of the electromagnet, one to the left and the other to the right. The right one was dyed with rhodamine B to induce visual differences. Upon turning on the electromagnets, the droplets move and mix on the top of the alloy core of the electromagnet. An LED was used to provide enough illumination for video recording (Cannon Repel T2i).

Mixing droplets without wrapping layers. FLIPS were prepared on porous PTFE membranes with 1-μm pore size to suppress the micro-topographical response. Fluorocarbon-based ferrofluid 2 diluted to 4% by volume with Krytox 100 was used. The FLIPS was placed in a plastic Petri dish, which was then filled with dodecane. Droplets (about 10 μl) of aqueous solution of sodium bicarbonate and hydrogen chloride were then placed on the FLIPS with a micro-pipette. A permanent magnet was used to induce a macroscopic response to push one droplet towards the other and mix them.

Adhesion and friction experiments. *Adhesion measurements on PTFE-membrane-based FLIPS.* FLIPS were prepared with a porous PTFE membrane with 20-μm pore size and fluorocarbon-based ferrofluids 1 and 2 without dilution to induce both micro-topographical and macro-topographical responses. As a result, the size of the macro-topographical protuberance and its ability to separate two surfaces spontaneously was influenced not only by the ferrofluid overlayer but also by the amount of ferrofluid extracted from the porous membrane. Adhesion measurements were performed on an Instron 5566 electromechanical testing system. A plastic sample holder was designed and 3D-printed to fit the gripper of the instrument and to provide a flat top surface with an area of 1 inch². The porous PTFE membrane was first attached to the top of the 3D-printed sample holder with double-sided tape and then 150 μl of ferrofluid was added. A glass cover slide, a polytetrafluoroethylene Teflon sheet (McMaster Carr, 0.015-inch thick, one side adhesive-ready) and a slippery liquid-infused porous surface (SLIPS) were attached to another sample holder. The FLIPS was positioned at the bottom and the test surface at the top. During testing, the FLIPS stayed stationary, and the test surface was first brought down at a speed of 0.1 mm s⁻¹ to be in contact with the FLIPS, held still for 10 s and then retracted at 0.01 mm s⁻¹, 0.1 mm s⁻¹ or 1 mm s⁻¹. Position $l = 0$ corresponds to the position where the top surface was pressed slightly against the FLIPS without squeezing ferrofluid out of the FLIPS. For each data point, a minimum of five measurements were performed.

Adhesion measurements on channel-like microstructure-based FLIPS. The microstructure of pattern 1 was used to demonstrate the anisotropic properties of FLIPS. The substrates were prepared with glass slide backing. Epoxy (EPO-TEK OG178) was cast onto the PDMS mould and then the glass slide was placed onto the epoxy, creating a homogeneous thin epoxy layer between the PDMS mould and the glass slide, and cured under UV light. The microstructured epoxy resin was then peeled off the mould, infiltrated with 100 μl of fluorocarbon-based ferrofluid 1 and spun at 500 r.p.m. for 60 s before being attached to another sample holder. The overlayer thickness was estimated to be about 20 μm. The adhesion measurements were performed on a customized set-up. The adhesion set-up was built on an inverted optical microscope (Axio Observer A1, Zeiss) with a video camera (Grasshopper3, Point Grey Research), enabling the recording of the contact interface. The adhesion force was measured by a sensitive load cell (GSO-25 and −1 K, Transducer Techniques) mounted on a computer-controlled high-precision piezo motion stage (LPS-65 2″, Physik Instrumente) in the z direction, with a resolution of 5 nm and a maximum velocity of 10 mm s⁻¹. Fine positioning in the x and y directions was done by a manual xy stage (NFP-2462CC, Positionierungstechnik Dr Meierling) and tilt correction was adjusted by two goniometers (M-GON65-U, Newport). Motion control of the piezo stages and data acquisition were performed using a customized Linux code (Ubuntu, Canonical). The program enabled control over preload, velocity, displacement in the x and z directions, and contact time. The load cell was linked to the computer via a signal conditioner (BNC-2110, National Instruments) and the voltage signal from the force measurement was transferred through a data acquisition board (PCIe-6259, National Instruments). A brass holder with attached plastic disk was prepared to attach the PDMS probe to the load cell. The circular plastic disk with 4-mm diameter and 1-mm thickness was laser-cut from a plastic plate and attached to the brass holder by a silicone adhesion promoter (Sil-Poxy, Smooth-On). The FLIPS was positioned at the bottom and the holder on top. Sylgard 184 prepolymer and curing agent with weight ratio of 10:1 were mixed, degassed and cast on a glass plate, and a thin film with 500-μm thickness was created by a film applicator (Multicator 411, Erichsen). The sample was cured in a vacuum oven at 90 °C for 1 h. Square PDMS probes with 5-mm side length were cut from a 500-μm-thick PDMS film and placed onto the FLIPS surface to ensure alignment. A vinylsiloxane polymer (Flexitime Medium Flow, Heraeus Kulzer) was used to bond the PDMS probe to the holder. The holder was

inked into the uncured vinylsiloxane polymer film, moved and contacted with the backside of the aligned PDMS probe with 50-mN compressive load. After 3 min, the vinylsiloxane polymer was polymerized and the probe bonded to the holder. During the adhesion testing, the FLIPS stayed stationary; the probe approached the surface at $50\,\mu m\,s^{-1}$ and was first brought in contact with a preload of 50 mN. After a contact time of 10 s, the probe was retracted at a speed of $10\,\mu m\,s^{-1}$, $100\,\mu m\,s^{-1}$ or $1{,}000\,\mu m\,s^{-1}$ until the probe was detached from the FLIPS. The probe was cleaned after each measurement with a particle-free tissue and isopropanol to remove accumulated ferrofluid. Pristine and representative positions of the different regions (H_0 off, R1, R2 and R3) were selected for each measurement. The ferrofluid was respread over the substrate surface with a magnet and the initial conditions were restored, and all pristine and representative positions were measured. The experiments were conducted in a temperature- and humidity-controlled laboratory with the conditions kept at 20–25 °C and 25%–35%, respectively. For each data point, a minimum of five measurements were performed.

Friction measurements on channel-like microstructure-based FLIPS. The FLIPS samples were prepared in the same way as in Methods subsection 'Adhesion measurements on channel-like microstructure-based FLIPS'. Friction measurements were performed on the same customized set-up. The load cell was attached to the z-direction piezo motion stage perpendicular to the FLIPS. A plastic holder was designed and laser cut to attach the PDMS film probe to the load cell and to provide aligned configuration. Sylgard 184 prepolymer and curing agent with a weight ratio of 10:1 were mixed, degassed and cast on a glass plate, and a thin film with 500-μm thickness was created by a film applicator (Multicator 411, Erichsen). The sample was cured in a vacuum oven at 90 °C for 1 h. The PDMS film probe with length of 25 mm was cut from a 500-μm-thick PDMS film. A 1-cm² PDMS piece was attached to the lower side of the film probe by a thin layer of silicone adhesion promoter to provide a constant contact area. The PDMS film probe was bonded to the plastic holder by a silicone adhesion promoter. The positioning in the x and y directions was done by a manual xy-stage and tilt was corrected by two goniometers to ensure parallel shear. During testing, the film probe stayed stationary and the FLIPS was sheared parallel at a constant velocity. The film probe approached the surface at $1{,}000\,\mu m\,s^{-1}$ and was brought in contact with the substrate. A constant load of 10 mN or 100 mN was applied. After a contact time of 10 s, the FLIPS was sheared over a distance of 5 mm and 10 mm with a velocity of $100\,\mu m\,s^{-1}$ and $1{,}000\,\mu m\,s^{-1}$. The probe was cleaned after each measurement with a particle-free tissue and isopropanol to remove accumulated ferrofluid. Pristine and representative positions of the different regions (H_0 off, R1, R2 and R3) were selected for each measurement. The ferrofluid was respread over the substrate surface with a magnet and the initial conditions were restored, and all pristine and representative positions were measured. The experiments were conducted in a temperature- and humidity-controlled laboratory, with the conditions kept at 20–25 °C and 25%–35%, respectively. For each data point, a minimum of five measurements were performed.

Demonstration of switchable adhesion. FLIPS were prepared on porous PTFE membranes with 20-μm pore size. Ferrofluid 2 was used to induce macro-topographical and micro-topographical responses. As a result, the size of the macro-topographical protuberance and its ability to separate two contacting surfaces spontaneously was influenced not only by the ferrofluid overlayer but also by the amount of ferrofluid extracted from the porous membrane. 3D models were created in Rhinoceros 3D with the aid of the Grasshopper plugin and were printed on Objet Connex 500. Before the experiment, the PTFE membrane was attached to the top of the white holding frame and the ferrofluid was added and spread using a magnet. A beaker was then placed insider the holding frame and the top handle was placed on the FLIPS. Three separate 0.5-inch-diameter and 0.5-inch-tall N52 NbFeB magnets were introduced manually to generate a topographical response. The macro-topographical protuberance (the size of which was determined not only by the ferrofluid overlayer but also by the amount of ferrofluid extracted from the microporous membrane, that is, the micro-topographical response) creates a gap that reduces the adhesion between the top handle and the bottom frame. The magnets were later removed with a magnetic stainless-steel tweezer.

Demonstration of switchable friction. FLIPS were prepared on porous PTFE membranes with 20-μm pore size. Ferrofluid 2 was used to induce macro-topographical and micro-topographical responses. As a result, the size of the macro-topographical protuberance and its ability to separate two contacting surfaces spontaneously was influenced not only by the ferrofluid overlayer but also by the amount of ferrofluid extracted from the porous membrane. 3D models were created in Rhinoceros 3D with the aid of the Grasshopper plugin and were printed on Objet Connex 500. A stepper motor (Lin Engineering, 3518M-07) was used to provide the rotation. Arduino Uno microcontroller with Adafruit motor shield was used to control the rotation of the stepper motor and interface it with a laptop PC. The 3D-printed set consisted of a bottom spinning wheel that was attached to the shaft of the stepper motor, a top spinning wheel and a top stationary wheel. The PTFE membrane was first attached to the top surface of the bottom spinning wheel and the ferrofluid was

added to the middle of the membrane. The top spinning wheel was then pressed against the bottom spinning wheel to spread the ferrofluid uniformly throughout the PTFE membrane. Two stacks of plastic Petri dishes and several plastic sheets were used to adjust the height of the top stationary wheel so it could constrain the position of the top spinning wheel. Four small black parts were attached to the top spinning wheel as a visual indicator of spinning and to adjust the overall friction during spinning. At the centre of the top spinning wheel, a 0.5-inch-wide hole was created to accommodate a stack of two 0.5-inch-diameter and 0.5-inch-tall N52 NbFeB magnets. During the demonstration, the movement of the stepper motor rotates the bottom spinning wheel, which rotates the top spinning wheel without magnets. When the magnets were placed in the hole in the top spinning wheel, the macro-topographical protuberance (the size of which was determined by not only the ferrofluid overlayer but also by the amount of ferrofluid extracted from the microporous membrane, that is, the micro-topographical response) creates a gap that reduces the friction between the top and the bottom spinning wheels and stops the rotation of the top spinning wheel. The explanatory animation at the end of Supplementary Video 8 was made in Maya, using the models created in Rhinoceros 3D.

Demonstration of pumping. Aeos extruded microporous ePTFE tubing (effective pore size of about 5–60 μm) and ferrofluid 2 were used to allow the ferrofluid to move in and out of the tubing pore wall. 3D-printed parts were used to construct the rest of the pump. 3D models were created in Rhinoceros 3D with the aid of the Grasshopper plugin and were printed on Objet Connex 500. The stepper motor (Lin Engineering, 3518M-07) was used to provide rotation. An Arduino Uno microcontroller with Adafruit motor shield was used to control the rotation of the stepper motor and interface it with a laptop PC. The 3D-printed set consisted of a flat top plate, a bottom plate with a circular track, two linear tracks to accommodate the movement of the ferrofluid protuberance and the tubing, and two spinning wheels, each with ten slots for 0.5-inch-diameter and 0.5-inch-tall magnets. Before the experiment, the ePTFE tube was first fitted into the track in the bottom plate and the ferrofluid was added at various locations along the circular track to wet the tube. Krytox 100 oil was added to various locations along the linear tracks to provide sealing for the liquid being pumped along the inlet and outlet parts of the tube. The top plate was then used to sandwich the tube and the sandwich structure was then placed on the top of the bottom spinning wheel, inside of which five magnets were positioned in the holes along the perimeter with even spacing. The top spinning wheel was then installed, into which another five magnets were placed. The explanatory animation at the end of Supplementary Video 9 was made in Maya, using models created in in Rhinoceros 3D.

Biofilm studies. *FLIPS preparation.* PTFE membranes with a pore size of 10 μm were adhered to a 50 mm × 75 mm glass slide using a thin layer of semi-cured PDMS (Sylgard 184 silicone elastomer Dow Corning Corporation), enabling the thorough attachment of the membrane to the glass slide without infiltrating the PTFE network with PDMS. After completing the PDMS curing in an oven (70 °C for 4 h), 500 μl of ferrofluid was added to the surface of each PTFE membrane and spread carefully using a ring magnet until all of the membrane area was fully infused with ferrofluid. The ferrofluids used in our study consisted of non-toxic components: iron oxide particles dispersed in fluorocarbon solvents. The non-toxicity of many fluorocarbon solvents is well known and manifested by the fact that they have even been used as the main ingredients in artificial blood substitutes (Fluosol) that are FDA-approved and used with human subjects. Iron oxide nanoparticles are also non-toxic, with some specific types FDA-approved as MRI contrast agents. This is in contrast to ferrofluids based on many other types of carrier fluids and nanoparticles, including nickel and cobalt, which are known to be toxic to biological matter.

Algae cultivation and experimental set-up. The green alga *Chlamydomonas reinhardtii* (UTEX number 89) from the University of Texas Culture Collection was used as a model organism to explore the biofilm disruption or detachment potential of FLIPS systems. *C. reinhardtii* was grown in a Soil Extract (Bristol-medium-based) solution under non-axenic conditions until the stock culture reached a density of approximately 10^7 cells ml^{-1}. This stock culture was diluted with fresh Soil Extract to a 1:5 ratio of stock culture to fresh medium. 80 ml of the diluted culture was added to square (10 cm × 10 cm) Petri dishes containing the prepared FLIPS treatments, allowing the algae to settle on test surfaces. The Petri dishes were then placed under a Sun Blaze T5HO fluorescent light fixture (Sunlight Supply) and were grown under a 16 h–8 h light–dark cycle at 24 °C for seven days until a cohesive green algae biofilm had formed. No negative effects of the ferrofluid on algae growth and biofilm formation were observed when compared with PTFE-only control treatments, and a healthy green algae biofilm remained stably attached to the surface until the magnetic actuation was performed, thus confirming the non-toxic nature of FLIPS.

Biofilm removal. To test the potential of FLIPS surfaces to disrupt or detach the adhered biofilm, a ring magnet was introduced immediately beneath the square Petri dishes containing the fouled FLIPS and the algae medium. The applied

magnetic fields then led to a concentration of the ferrofluid beneath the magnet, breaking up the adhered green algae biofilm in the process. Moving the magnet up and down the slide caused a 'ferrofluid wave' to travel over the FLIPS, detaching and concentrating the biofilm. The aggregations of biofilms moved along with the ferrofluid wave but did not mix with the underlying ferrofluid. After removing the magnet, the Petri dishes were shaken gently to see if the biofilm remnants were still associated with the ferrofluid. The biofilm threads were not associated, but instead lifted off the FLIPS and started floating freely into the algae media. By contrast, simple shaking of the Petri dishes without magnetic actuation did not result in any biofilm detachment from the FLIPS surface. Control PTFE treatments that did not contain any ferrofluid showed no response to the magnetic actuations and the green algae biofilms remained firmly attached to the surface of the controls.

Simulations and calculations. Simulations of magnetic fields and magnetic pressures were performed with COMSOL. The data for the ferrofluid M–H curve were obtained from Ferrotec. Calculation of the force density was performed with OriginLab. Calculations of van der Waals energy and disjoining pressure were performed with Mathematica.

Code availability. The codes used in analysing videos and other data are available from the corresponding author.

Additional notes on the scaling relations of the micro-topographical response of FLIPS. Using the geometry in Fig. 1b, the pressure gradient in the x direction drives the flow and is resisted by viscous dissipation in the z direction; therefore, using the lubrication approximation[37,38], we have

$$\frac{\partial p_\gamma}{\partial x} = \eta \frac{\partial^2 U}{\partial z^2}$$

where $p_\gamma \approx 2\gamma/d_y$ is the capillary pressure and $U \approx dL_x/dt \approx L_x/t$. The left-hand side represents the capillary pressure gradient (which drives the porous-capillary flow) and the right-hand side represents the viscous dissipation. Using the approximations $\partial p_\gamma/\partial x \approx p_\gamma/L_x \approx 2\gamma/d_y L_x$ and $\partial^2 U/\partial z^2 \approx U/h_0^2 \approx L_x/(th_0^2)$ and rearranging the terms gives the scaling relation

$$L_x \approx \left(\frac{2\gamma h_0^2}{\eta d_y}\right)^{1/2} t^{1/2}$$

Putting numerical values in the above equation and setting the units of L_x as millimetres and t as seconds gives $L_x \approx 0.35 t^{1/2}$. This derivation gives the same power law as in equation (2). The only difference is the pre-factor.

A second alternative is to use magnetic pressure to replace the capillary pressure term:

$$\frac{\partial |p_m|}{\partial x} = \eta \frac{\partial^2 U}{\partial z^2}$$

where $|p_m| \approx \mu_0 M_s H_0$. This replacement represents the incorporation of the actual driving force—the magnetic pressure gradient—in the formulation of the scaling relation. Arranging terms gives the scaling relation

$$L_x \approx \left(\frac{|p_m| h_0^2}{\eta}\right)^{1/2} t^{1/2}$$

Using $p_m \approx 10^4$ Pa and again setting the units of L_x as millimetres and t as seconds gives $L_x \approx 5.6 t^{1/2}$.

The derivations in the main text and here all give the same power law, and differ only in the pre-factors. A more accurate model will need to combine these models: near the magnet, it is primarily the magnetic force that drives the flow; far from the magnet, it is the capillary pressure gradient that drives the flow. In addition, these scaling derivations are essentially 2D models; they omit the 3D nature of the geometry of the microstructure. We are currently developing numerical models to take into account all of the considerations stated above.

Additional notes on the formation of the wrapping layer. The estimate of the formation of the wrapping layers based on the calculation of the (initial) spreading coefficients does not correlate with our experiments (Extended Data Fig. 4, Extended Data Table 2). This method is derived from work in the early 1920s[39,40]. It was also the method of choice in recent studies on wrapping layers[22,41]. We adopt the term 'initial spreading coefficient' S_i to denote the value that we calculate[42] and reserve the term 'spreading coefficient' to mean the 'true equilibrium spreading coefficient'[42]. The main source of discrepancy for the S_i approach is that interfacial tensions are very sensitive to trace amounts of surface-active agents, especially for a water–hydrocarbon interface. Any additives such as dyes or even air-borne dust particles can alter the water–hydrocarbon interfacial tension sufficiently to change the signs of S_i.

Our estimate of the formation of the wrapping layer is based on the calculations of long-range van der Waals interactions[23–26,38,43]. The origin of these interactions is different from that of the surface tension (which is due to short-range intermolecular forces) and represents the interaction between the two media across the wrapping layer (hence long-range). If this interaction between the two media is attractive, then the wrapping layer is absent; if this interaction is repulsive, then the wrapping layer is formed. Knowing the sign of this interaction enables us to estimate the stability of the wrapping layer (in other words, the absence or presence of the wrapping layer). From the perspective of thin films, a ferrofluid thin film is stable between water and air because the repulsive van der Waals interaction between air and water tends to thicken it; on the other hand, a ferrofluid thin film is unstable between water and hydrocarbon because the attractive van der Waals interaction between water and hydrocarbon tends to thin it.

We provide below three methods to estimate the sign of these long-range van der Waals interactions, in order of increasing complexity: (1) using combining relations (Extended Data Table 3); (2) using non-retarded Hamaker constants based on Lifshitz theory (Extended Data Table 4); and (3) using Hamaker constants with a relativistic retardation correction based on Lifshitz theory (Extended Data Fig. 5).
Method 1. We estimate the signs of the Hamaker constants A_{132} and van der Waals interaction energy G_{132} using combining relations[24,25] (results are presented in Extended Data Table 3):

$$A_{132} = \left(\sqrt{A_{11}} - \sqrt{A_{33}}\right)\left(\sqrt{A_{22}} - \sqrt{A_{33}}\right)$$
$$\approx 24\pi\delta_0^2\left(\sqrt{\gamma_1^D} - \sqrt{\gamma_3^D}\right)\left(\sqrt{\gamma_2^D} - \sqrt{\gamma_3^D}\right)$$
$$G_{132} = -\frac{A_{132}}{12\pi d^2} \approx -\left(\sqrt{\gamma_1^D} - \sqrt{\gamma_3^D}\right)\left(\sqrt{\gamma_2^D} - \sqrt{\gamma_3^D}\right)$$

where A_{ijk} is the Hamaker constant for the interaction between medium i and medium k across medium j, G_{ijk} is the van der Waals interaction energy for the interaction between medium i and medium k across medium j, A_{ii} is the Hamaker constant for the interaction between medium i across vacuum, δ_0 is the atomic cut-off distance (a constant), γ_i^D is the dispersive component of the surface tension of medium i and d is the thickness of the intermediate medium. For hydrocarbons and ferrofluids, γ_i^D is equal to the surface tensions in air; for water, $\gamma_i^D \approx 22$ mN m^{-1} (refs [25,43]).

This calculation used the physical properties of fluorocarbon-based ferrofluids and perfluoropolyether oil (Krytox 100) provided by the manufacturers and the measured surface and interfacial tensions of liquids used in the study (Extended Data Table 1).
Method 2. We estimate the non-retarded Hamaker constants A_{132} and van der Waals interaction energy G_{132} using Lifshitz theory (results are presented in Extended Data Table 4). The calculations are based on the following equation, adapted from ref.[24]:

$$A_{total} = A_{\nu=0} + A_{\nu>0}$$
$$\approx \frac{3}{4}kT\left(\frac{\varepsilon_1 - \varepsilon_3}{\varepsilon_1 + \varepsilon_3}\right)\left(\frac{\varepsilon_2 - \varepsilon_3}{\varepsilon_2 + \varepsilon_3}\right)$$
$$+ \frac{3h\nu_e}{8\sqrt{2}}\frac{(n_1^2 - n_3^2)(n_2^2 - n_3^2)}{(n_1^2 + n_3^2)^{1/2}(n_2^2 + n_3^2)^{1/2}[(n_1^2 + n_3^2)^{1/2} + (n_2^2 + n_3^2)^{1/2}]}$$
$$G_{132} = -\frac{A_{132}}{12\pi d^2}$$

where ε_i is the static dielectric constant of medium i, n_i is the refractive index of medium i, ν_e is the main electronic absorption frequency at about 3×10^{15} Hz, k is the Bolzmann constant, T is temperature, h is the Planck contant, and the subscript ν is the absorption frequency.

A_{total} is dominated by the dispersive term $A_{\nu>0}$, so we can use refractive indexes alone to predict the sign of the van der Waals interaction energy in our droplet-on-FLIPS systems. In addition, the calculations use the dielectric constants and refractive indices of the solvents of the ferrofluids or, in the case of 4 vol% ferrofluid, the properties of Krytox 100. This assumption is justified on the grounds that nanoparticles of iron oxides are shielded by fluorocarbon surfactants or polymers and that their van der Waals interactions with other media are therefore greatly reduced. The dominant role of dispersive forces is in the surface tension of pure ferrofluid: the dispersive components of the surface tension of ferrofluids 1 and 2 are estimated to be 13.7 mN m^{-1} and 12.4 mN m^{-1}, respectively, using $\gamma_i^D = A_{ii}/[24\pi(0.165 \text{ nm})^2]$.

This method provides the same (correct) prediction for the formation of the wrapping layer as does the method in Extended Data Table 3. In essence, these calculations reflect the excess polarizability, or relative polarizability, of different phases: fluorocarbon is less polarizable than water or hydrocarbon, but more polarizable than air (vacuum)[23,38]. The physical constants of water, dodecane and air used are: $\varepsilon_{water} = 80$, $n_{water} = 1.333$; $\varepsilon_{dodecane} = 2.01$, $n_{dodecane} = 1.411$; and $\varepsilon_{air} = 1$, $n_{air} = 1$.

Method 3. We estimate the Hamaker constants A_{132} with relativistic retardation correction, the van der Waals interaction energy G_{132} and the disjoining pressure (results are presented in Extended Data Fig. 5). The calculations are based on the following equations, which are adapted from ref. [23]:

$$\varepsilon_i(i\xi_n) = 1 + \frac{n_i^2 - 1}{1 + (\xi_n/\omega_{UV})^2}, \quad i = 1, 2, 3$$

$$\xi_n = \frac{2\pi kT}{\hbar} n, \quad n = 1, 2, 3, 4\dots$$

$$R(l) = (1 + r_n)e^{-r_n}$$

$$r_n(l) = \frac{2l}{c/[\varepsilon_3(i\xi_n)]^{1/2}}\xi_n$$

$$A_{132}(l) = \frac{3kT}{2}\sum_{\xi_n}\left[\frac{\varepsilon_1(i\xi_n) - \varepsilon_3(i\xi_n)}{\varepsilon_1(i\xi_n) + \varepsilon_3(i\xi_n)}\right]\left[\frac{\varepsilon_2(i\xi_n) - \varepsilon_3(i\xi_n)}{\varepsilon_2(i\xi_n) + \varepsilon_3(i\xi_n)}\right]R(l)$$

$$G_{132}(l) = -\frac{A_{132}(l)}{12\pi l^2}$$

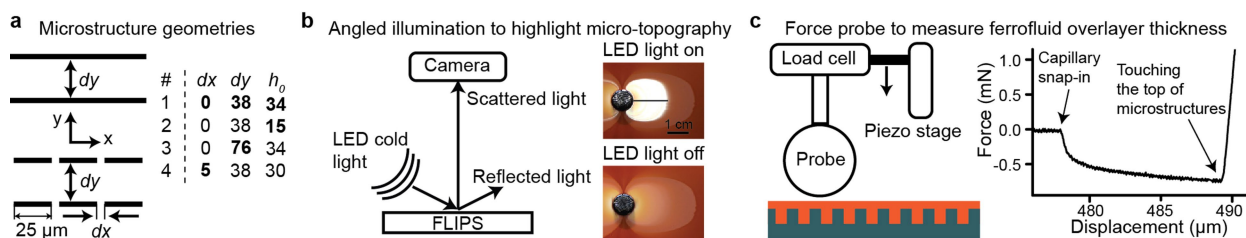$$p_{dis} = -\frac{\partial G_{132}(l)}{\partial l}$$

where, $\varepsilon_i(i\xi_n)$ is the dielectric response of medium i at imaginary frequency $i\xi_n$ and ξ_n are the sampling frequencies, or 'Matsubara frequencies'; $R(l)$ and $r_n(l)$ account for the retardation of van der Waals interactions over a distance l due to the finite velocity of electromagnetic waves; and $A_{132}(l)$ is the Hamaker constant for medium configuration 1–3–2, $G_{132}(l)$ is the corresponding van der Waals interaction energy and p_{dis} is the corresponding disjoining pressure.

This method is most useful when studing the thickness-dependent properties of wrapping layers, such as meta-stability, and can be extended to investigate the fine balances between disjoining, capillary and magnetic pressure.

Data availability. The datasets generated and analysed during this study are available from the corresponding author.

35. Pokroy, B., Epstein, A. K., Persson-Gulda, M. C. M. & Aizenberg, J. Fabrication of bioinspired actuated nanostructures with arbitrary geometry and stiffness. *Adv. Mater.* **21**, 463–469 (2009).
36. Kim, P., Adorno-Martinez, W. E., Khan, M. & Aizenberg, J. Enriching libraries of high-aspect-ratio micro- or nanostructures by rapid, low-cost, benchtop nanofabrication. *Nat. Protocols* **7**, 311–327 (2012).
37. Acheson, D. J. *Elementary Fluid Dynamics* Ch. 7 (Oxford Univ. Press, New York, 1990).
38. de Gennes, P.-G., Brochard-Wyart, F. & Quéré, D. *Capillarity and Wetting Phenomena: Drops, Bubbles, Pearls, Waves* Ch. 4 (Springer, Berlin, 2004).
39. Hardy, W. B. The tension of composite fluid surfaces and the mechanical stability of films of fluid. *Proc. R. Soc. Lond. A* **86**, 610–635 (1912).
40. Hardy, W. B. The tension of composite fluid surfaces.—No. II. *Proc. R. Soc. Lond. A* **88**, 313–333 (1913).
41. Smith, J. D. et al. Droplet mobility on lubricant-impregnated surfaces. *Soft Matter* **9**, 1772–1780 (2013).
42. Bonn, D., Eggers, J., Indekeu, J., Meunier, J. & Rolley, E. Wetting and spreading. *Rev. Mod. Phys.* **81**, 739–805 (2009).
43. Fowkes, F. M. Attractive forces at interfaces. *Ind. Eng. Chem.* **56**, 40–52 (1964).

a Microstructure geometries

#	dx	dy	h_0
1	0	38	34
2	0	38	15
3	0	76	34
4	5	38	30

b Angled illumination to highlight micro-topography

c Force probe to measure ferrofluid overlayer thickness

Extended Data Fig. 1 | Microstructure geometries and techniques for studying the dynamics of the topographical responses of FLIPS.
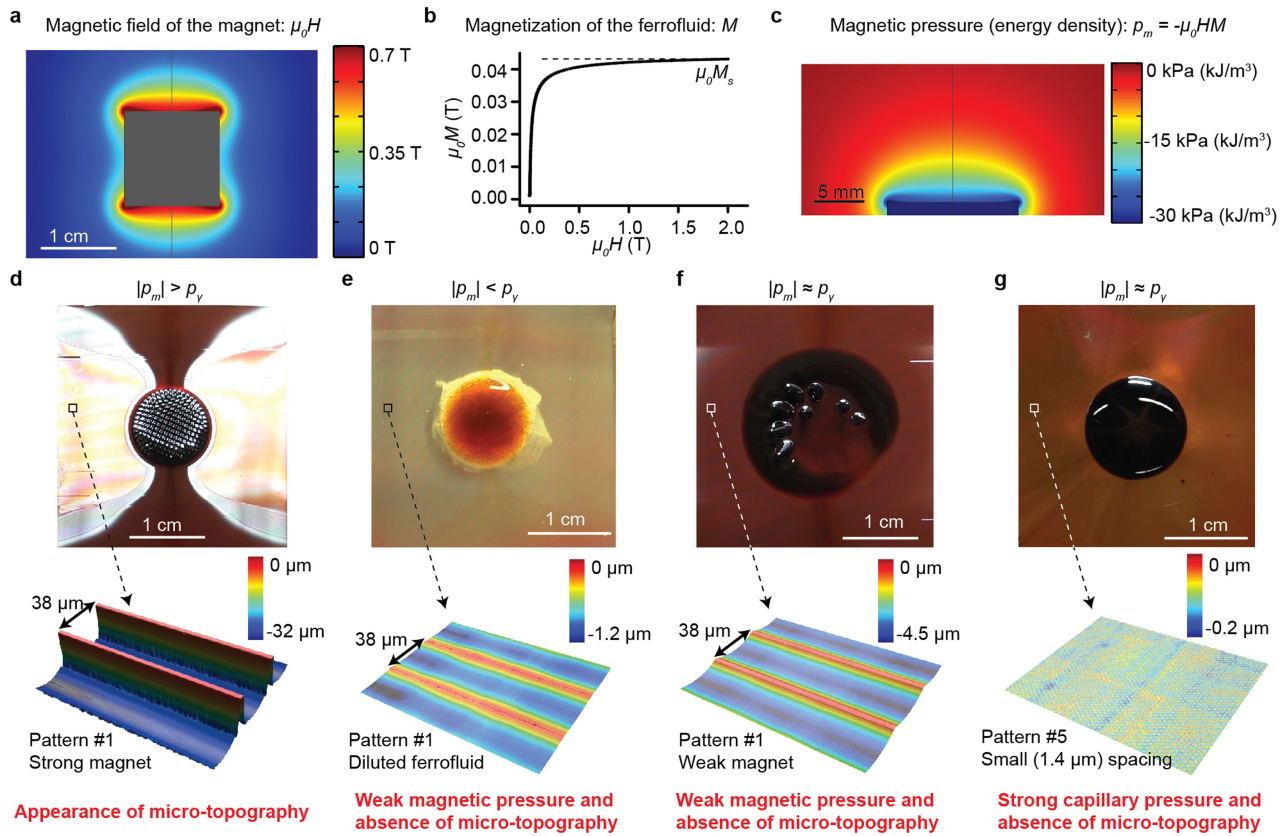**a**, Microstructure geometries used in the scaling analysis of the dynamics of micro-topographical response: arrays of microchannels (1–3) and an array of microplates (4). The comparisons between 1 and 2–4 show the influence of h_0, d_y and d_x, respectively. **b**, Angled illumination technique to highlight the micro-topographical region. A cold LED line light (Zeiss CL 6000 and line light S) illuminates the FLIPS sample from an incidence angle of about 30° to induce scattering from the micro-topographical region. The contrast due to the high brightness produced from the scattering facilitates the colour thresholding step in the video processing.

The two images on the right show a comparison with and without the LED. **c**, Force-probe technique to measure the thickness of the ferrofluid overlayer. The diagram on the left is a schematic of the set-up. A spherical probe connected to a load cell is lowered slowly onto the FLIPS surface through the motion of a piezo stage. The speed of the approach ($10\,\mu m\,s^{-1}$) and the sampling rate of the load cell (1 ms) determine the limit of the measurement resolution (10 nm). The plot on the right is a representative force–displacement curve from the measurement. The overlayer thickness is the distance between the capillary snap-in (the moment the probe touches the top of the overlayer) and the beginning of the steep increase in the force (the moment the probe touches the top of the microstructures).
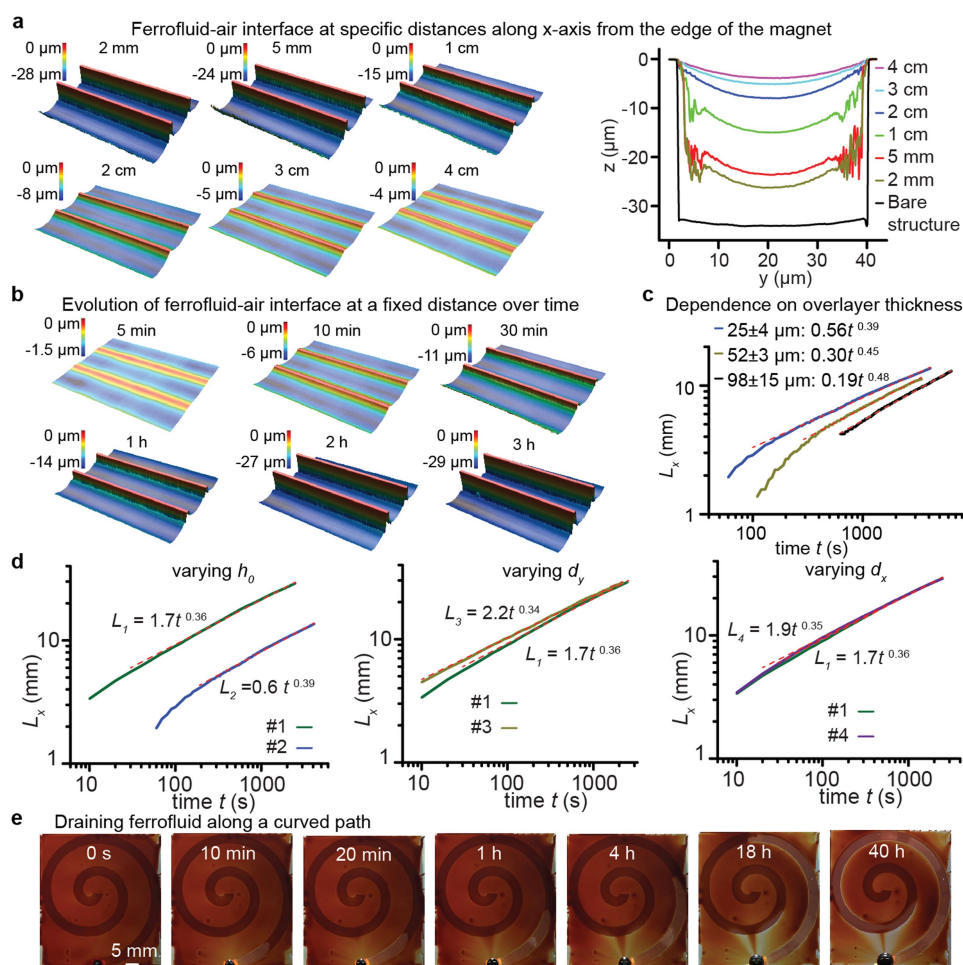
Extended Data Fig. 2 | Profiles of ferrofluid–air interfaces measured by a 3D laser-scanning confocal microscope, the dependence of the scaling relations on the overlayer thickness, and draining ferrofluid along a curved path. a, 3D profiles of the ferrofluid–air interface measured along the x axis at various distances from the edge of the magnet (labelled). The profiles show a gradual increase in the ferrofluid level inside the channel along the x axis, which corresponds to a gradual decrease in interfacial curvature. Measurements were performed on a 1 inch × 3 inch FLIPS sample after 2 h. Pattern 1 was used, and the channel direction was aligned to the long side of the FLIPS sample. On the right is a plot of the cross-sectional profiles of the ferrofluid–air interface. The signal is noisy in the high-curvature region near the edge, owing to the limit of the numerical aperture of the 100× long-working-distance objective used. **b**, 3D profiles of ferrofluid–air interface measured 1.5 cm away from the edge of the magnet over time (labelled). The FLIPS sample is the same as in **a**. The profiles show a gradual decrease in ferrofluid level inside the channel, which corresponds to a gradual increase in interfacial curvature. The corresponding plots of the cross-sectional profiles are presented in Fig. 1c. **c**, Dependence of the scaling relations on the overlayer thickness. Pattern 2 was used. Increasing the overlayer thickness decreases the prefactor but increases the power in the scaling relations. **d**, Effects of varying h_0, d_y and d_x on the scaling relations. The overlayer thicknesses are roughly 10–20 μm. **e**, Draining of ferrofluid along a curved path in a spiral pattern, demonstrating the ability of the porous-capillary flow to make turns.

a Magnetic field of the magnet: $\mu_0 H$

0.7 T
0.35 T
0 T

1 cm

b Magnetization of the ferrofluid: M

$\mu_0 M$ (T)

0.04
0.03
0.02
0.01
0.00

$\mu_0 M_s$

0.0 0.5 1.0 1.5 2.0
$\mu_0 H$ (T)

c Magnetic pressure (energy density): $p_m = -\mu_0 HM$

0 kPa (kJ/m³)
-15 kPa (kJ/m³)
-30 kPa (kJ/m³)

5 mm

d $|p_m| > p_\gamma$

1 cm

38 μm

0 μm
-32 μm

Pattern #1
Strong magnet

Appearance of micro-topography

e $|p_m| < p_\gamma$

1 cm

38 μm

0 μm
-1.2 μm

Pattern #1
Diluted ferrofluid

Weak magnetic pressure and absence of micro-topography

f $|p_m| \approx p_\gamma$

1 cm

38 μm

0 μm
-4.5 μm

Pattern #1
Weak magnet

Weak magnetic pressure and absence of micro-topography

g $|p_m| \approx p_\gamma$

1 cm

0 μm
-0.2 μm

Pattern #5
Small (1.4 μm) spacing

**Strong capillary pressure and absence of micro-topography**

Extended Data Fig. 3 | Simulation of magnetic pressure and fine-tuning of the balance between magnetic and capillary pressure to create or conceal the micro-topography of FLIPS. a, Simulated magnetic field $B = \mu_0 H_0$ in free space surrounding a 0.5-inch-tall and 0.5-inch-diameter NdFeB magnet. **b**, Magnetization curve of ferrofluid 1 (from Ferrotec). The ferrofluid rapidly reaches its saturation magnetization $\mu_0 M_s \approx 0.04$ T. The saturation magnetization is regarded as a linear function of ferrofluid concentration in the following estimate. **c**, Magnetic pressure of ferrofluid 1 in the region above the magnet. The magnetic pressure (in kPa) can be considered as the magnetic energy density (in kJ m⁻³). Ferrofluid flows from a high pressure (energy) region to a low pressure (energy) region. **d**, Turning on the micro-topographical response; $|p_m| \approx 10^4$

Pa $> 10^3$ Pa $\approx p_\gamma$. **e–g**, Turning off the micro-topographical response. **e**, Response when the ferrofluid is diluted to 4% by volume; $|p_m| \approx 10^2$ Pa $< 10^3$ Pa $\approx p_\gamma$. **f**, Response using a weaker magnet (Alnico); $|p_m| \approx 10^3$ Pa $\approx 10^3$ Pa $\approx p_\gamma$. **g**, The distance between the repeating units of the microstructure is reduced so that the capillary pressure increases; $|p_m| \approx 10^4$ Pa $\approx 10^4$ Pa $\approx p_\gamma$. The microstructure is pattern 5, which is a hexagonal array of posts of 1.5 μm in diameter and about 10 μm in height. The spacing between posts is 1.4 μm. The bottom panels in **d–g** show the corresponding 3D profiles of the ferrofluid–air interface near the magnet. Only in d is the interface pulled down towards the bottom of the microstructure.
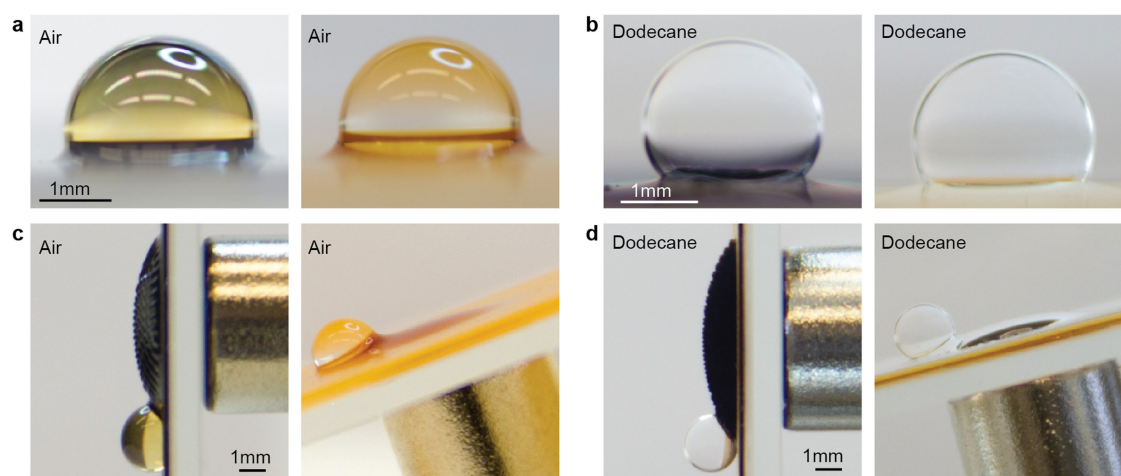
Extended Data Fig. 4 | Wrapping layers around a water droplet in air and in a hydrocarbon on FLIPS, and the ability of the macroscopic protuberance to hold a droplet at tilt angles. a, Photographs of a water droplet (about 5 μl) placed on a FLIPS with ferrofluid 1 (left) and diluted ferrofluid 1 (right). **b**, Photographs of a water droplet (about 5 μl) placed on a FLIPS with ferrofluid 1 (left) and diluted ferrofluid 1 (right) immersed in dodecane. **c**, Photographs of a water droplet (about 5 μl) held by a magnet at about 90° and 30° on a FLIPS with ferrofluid 1 (left) and diluted ferrofluid 1 (right), respectively. **d**, Photographs of a water droplet (about 5 μl) immersed in dodecane and held by a magnet at about 90° and 30° on a FLIPS with ferrofluid 1 (left) and diluted ferrofluid 1 (right), respectively. The comparison between **c** and **d** suggests that holding a droplet on the macroscopic protuberance does not require the existence of the wrapping layer and that capillary force is likely to dominate the interaction.
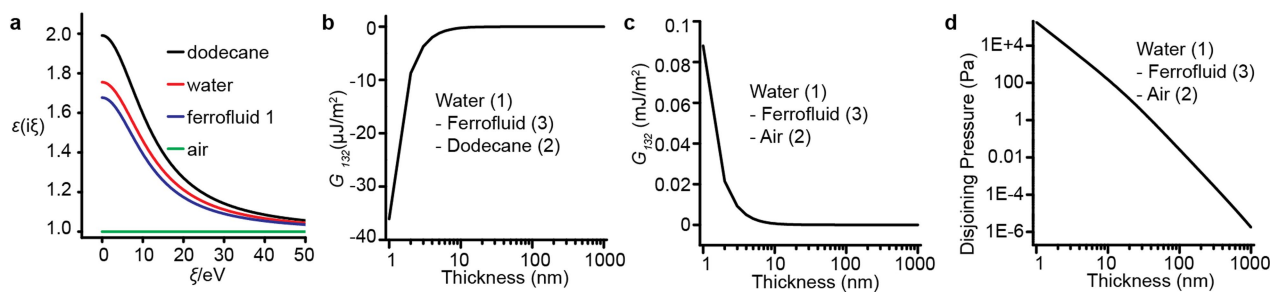
Extended Data Fig. 5 | Calculations of the van der Waals interaction energy G_{132} and disjoining pressure. a, Dielectric response ε as a function of imaginary frequency ξ for the four phases in the droplet-on-FLIPS system. The ferrofluid line lies between air and water, but below both water and dodecane. **b**, Interaction energy as a function of the thickness of the ferrofluid wrapping layer for the water–ferrofluid–dodecane configuration. The energy decreases as the thickness decreases, indicating that the wrapping layer is unstable. **c**, Interaction energy as a function of the thickness of the ferrofluid wrapping layer for the water–ferrofluid–air configuration. The energy decreases as the wrapping layer thickness increases, indicating that the wrapping layer is stable. **d**, Disjoining pressure as a function of the thickness of the ferrofluid wrapping layer in the water–ferrofluid–air system. The pressures are positive, indicating the formation of a stable thin film or a stable wrapping layer.
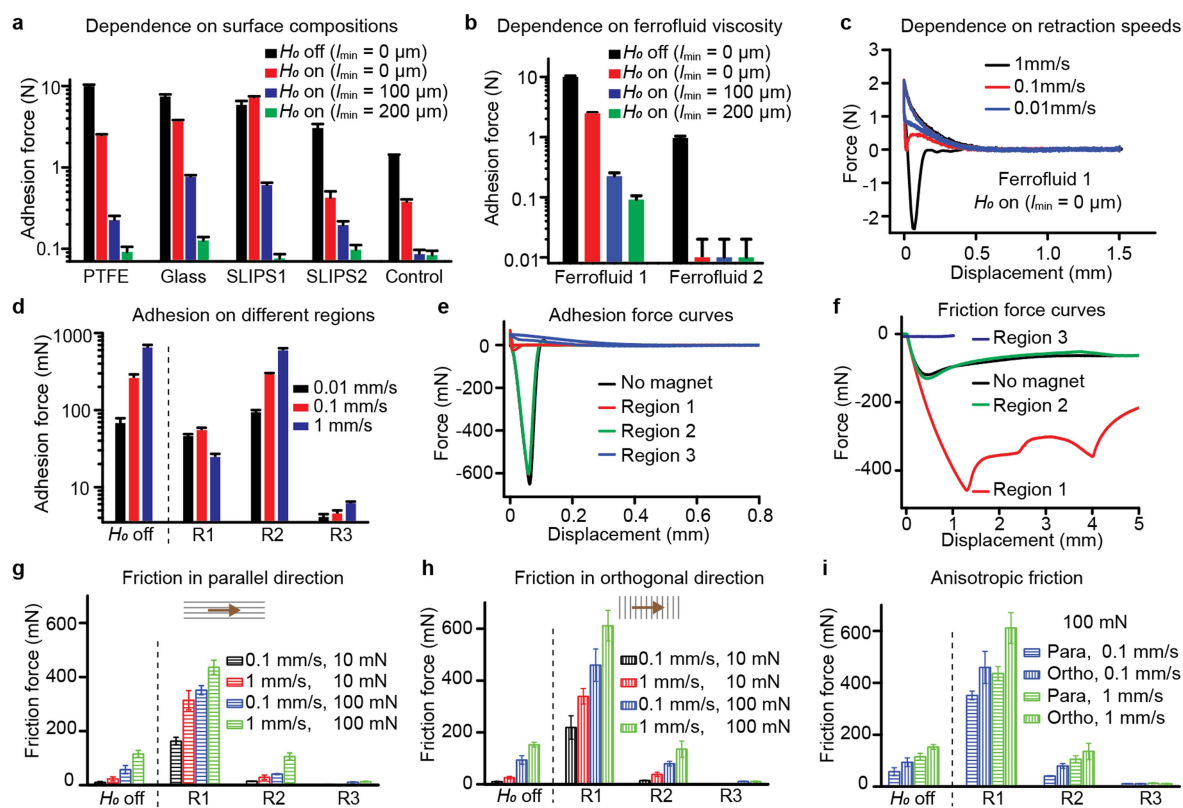
Extended Data Fig. 6 | Additional adhesion and friction data.
a–c, Adhesion measured on FLIPS prepared with isotropic porous Teflon membrane substrates. l_{min} is the minimum distance between the test surface and the FLIPS, as shown in the schematics in Fig. 4a. **a**, Adhesion of FLIPS on a low-energy surface (PTFE), a high-energy surface (glass) and two composite surfaces: a fluorocarbon-oil-based SLIPS (SLIPS1) and a silicone-oil-based SLIPS (SLIPS2). The control is measured between two glass surfaces coated with ferrofluid only and without the porous membrane. **b**, Dependence of adhesion on ferrofluid viscosity. Ferrofluid 1 ($\mu = 0.367$ Pa s) is more viscous than ferrofluid 2 ($\mu = 0.040$ Pa s). **c**, Dependence of adhesion on retraction speed. The adhesion decreases with decreasing retraction speed. The test surface is a PTFE surface. Panels **b** and **c** suggest that viscous adhesion is the dominant adhesion mechanism. **d–i**, Adhesion and friction measurements on FLIPS with anisotropic substrates. Pattern 1 is used. The numbering of regions (R1, micro-topography; R2, flat region with a ferrofluid overlayer; R3, macro-topography) is the same as in Fig. 1. **d**, Adhesion without a magnet and on different regions with a magnet at three different retraction speeds. **e**, Sample adhesion force curves measured at 1 mm s^{-1}. **f**, Sample friction

force curves measured at 1 mm s^{-1} and with 100-mN load. The value of the friction force is extracted from the lowest point along the curve. Note a signature of friction in the micro-topographical area of FLIPS, which is much higher than that on either flat or macro-topographical areas, characteristic of typical ferrofluid-coated non-structured surfaces. **g**, Friction forces without magnets and on different regions with a magnet in the direction parallel to the microchannels. Friction is highest in region 1, in the presence of micro-topography, and lowest in region 3, in the presence of macro-topography. The friction in region 2, with a flat fluid overlayer, is the same as for the entire FLIPS surface with no magnetic force. The difference can be as high as two orders of magnitude between regions 1 and 3, and one order of magnitude between region 1 and 2 (or between region 1 and with no magnetic force). **h**, The corresponding friction forces in the orthogonal direction. **i**, Direct comparison of friction forces in the parallel and orthogonal directions. The error bars in all panels correspond to the standard deviations, calculated from a minimum of five measurements. For details, see Methods section 'Adhesion and friction experiments'.

Extended Data Table 1 | Physical properties of fluorocarbon-based ferrofluids and perfluoropolyether oil (Krytox 100) provided by the manufacturers, and surface and interfacial tensions of liquids used here

Name	Density (g/cm^3)	Dielectric Constant ε	Refractive Index n	Dynamic Viscosity (Pa·s)	Kinematic Viscosity (cm^2·s^{-1})	Volatility	Magnetic Saturation (Gauss)
FC Ferrofluid 1	1.8 - 2.0	2.0*	1.295*	0.367	1.9	0.5% at 100 °C after 3.5h	400
FC Ferrofluid 2	1.7 - 1.9	1.94*	1.28*	0.040	0.22	72.3% at 100 °C after 1.5h	400
Krytox 100	1.87	2.2	1.3	0.013	0.070	87% at 121 °C after 22h	-

Interfaces	Interfacial Tension (mN/m) ‡	Interfaces	Interfacial Tension (mN/m)
Water – air	73.4±0.2	FF 1 – water	42.9±0.7
Dodecane – air	25.3±0.1	FF 2 – water	37.4±0.6
FF 1 – air	17.1±0.2	4v% FF 1 – water	57.5±0.6
FF 2 – air	13.5±0.1	4v% FF 2 – water	55.3±0.8
4v% FF 1 – air†	16.0±0.4	FF 1 – dodecane	6.7±0.2
4v% FF 2 – air	15.6±0.5	FF 2 – dodecane	4.8±0.1
Dodecane – water	44.8±0.1#	4v% FF 1 – dodecane	6.6±0.2
		4v% FF 2 – dodecane	7.1±0.1

FC, fluorocarbon-based; FF, ferrofluid.
*Dielectric constants and refractive indices of pure solvents.
#The interfacial tension of a dodecane–water interface is highly sensitive to trace amounts of impurities: the value listed is for dodecane of reagent-plus grade from Aldrich; other measured values include 52.2 ± 0.8 mN m^{-1} for analytical-standard grade from Aldrich and 45.7 ± 1.0 mN m^{-1} for 99+% grade from Alpha Aesar.
†v% represents percentage by volume.
‡The errors correspond to the standard deviations, calculated from at least six measurements. For details, please see Methods section 'Control of the wrapping layer formation and droplet mixing'.

Extended Data Table 2 | Initial spreading coefficients

Interface 1-2 (γ_{12})	Interface 3-1 (γ_{31})	Interface 3-2 (γ_{32})	Initial Spreading Coefficient $S_i = \gamma_{12} - (\gamma_{31} + \gamma_{32})$ (mN/m) *	Agreement with Experiments
Air – water	FF 1 – air	FF 1 – water	13.4	Yes
Air – water	FF 2 – air	FF 2 – water	22.5	Yes
Air – water	4v% FF 1 – air	4v% FF 1 – water	-1.2	No
Air – water	4v% FF 2 – air	4v% FF 2 – water	2.5	Yes
Dodecane – water	FF 1 – dodecane	FF 1 – water	-4.8	Yes
Dodecane – water	FF 2 – dodecane	FF 2 – water	2.6	No
Dodecane – water	4v% FF 1 – dodecane	4v% FF 1 – water	-19.3	Yes
Dodecane – water	4v% FF 2 – dodecane	4v% FF 2 – water	-17.6	Yes

*$S_i > 0$ indicates spreading; $S_i < 0$ indicates no spreading.

Extended Data Table 3 | The signs of Hamaker constants A_{132} and van der Waals interaction energy G_{132} estimated from combining relations

Medium 1	Medium 3	Medium 2	Hamaker Constant A_{132}	van der Waals interaction energy G_{132} *	Agreement with Experiments
Air	FF 1	Water	<0	>0 (Repulsive)	Yes
Air	FF 2	Water	<0	>0 (Repulsive)	Yes
Air	4v% FF 1	Water	<0	>0 (Repulsive)	Yes
Air	4v% FF 2	Water	<0	>0 (Repulsive)	Yes
Dodecane	FF 1	Water	>0	<0 (Attractive)	Yes
Dodecane	FF 2	Water	>0	<0 (Attractive)	Yes
Dodecane	4v% FF 1	Water	>0	<0 (Attractive)	Yes
Dodecane	4v% FF 1	Water	>0	<0 (Attractive)	Yes

*Only the sign of the van der Waals interaction energy is needed to predict the formation or absence of the wrapping layer.

Extended Data Table 4 | Non-retarded Hamaker constants A_{132} and van der Waals interaction energy G_{132} based on Lifshitz theory

Medium 1 – 3 – 2	$A_{v=0}$ (J)	$A_{v>0}$ (J)	A_{Total} (J)	van der Waals interaction energy G_{132}	Agreement with Experiments
Air – FF1 – Water	- 9.8x10^{-22}	- 3.1x10^{-21}	- 4.1x10^{-21}	>0 (Repulsive)	Yes
Air – FF2 – Water	- 9.4x10^{-22}	- 4.2x10^{-21}	- 5.1x10^{-21}	>0 (Repulsive)	Yes
Air – 4v% FF1 – Water	- 1.1x10^{-21}	- 2.7x10^{-21}	- 3.8x10^{-21}	>0 (Repulsive)	Yes
Air – 4v% FF2 – Water	- 1.1x10^{-21}	- 2.7x10^{-21}	- 3.8x10^{-21}	>0 (Repulsive)	Yes
Dodecane – FF1 – Water	7.3x10^{-24}	1.2x10^{-21}	1.2x10^{-21}	<0 (Attractive)	Yes
Dodecane – FF2 – Water	5.2x10^{-23}	1.8x10^{-21}	1.9x10^{-21}	<0 (Attractive)	Yes
Dodecane – 4v% FF1 – Water	- 1.3x10^{-22}	9.6x10^{-22}	8.3x10^{-22}	<0 (Attractive)	Yes